Vanadium metal-organic frameworks derived VOx/Carbon nano-sheets and paperclip-like VOx/nitrogen-doped carbon nanocomposites for sodium-ion battery electrodes

Vanadium metal-organic frameworks derived VO_x/Carbon nano-sheets and paperclip-like VO_x/nitrogen-doped carbon nanocomposites for sodium-ion battery electrodes

David Skoda[a,*], Tomas Kazda [b], Barbora Hanulikova[a], Ondrej Cech[b], Vit Vykoukal[c], Jan Michalicka[d], Pavel Cudek[b], Ivo Kuritka[a]

[a] *Centre of Polymer Systems, Tomas Bata University in Zlin, tr. Tomase Bati 5678, Zlin, CZ, 76001, Czech Republic*

[b] *Department of Electrical and Electronic Technology, Faculty of Electrical Engineering and Communication, Brno University of Technology, Technicka 10, Brno, CZ, 616 00, Czech Republic*

[c] *Central European Institute of Technology, Masaryk University, Kamenice 5, 625 00, Brno, Czech Republic d Central European Institute of Technology, Brno University of Technology, Purkynova 123, 612 00, Brno, Czech Republic*

** Corresponding author. E-mail address: dskoda@utb.cz (D. Skoda).*

HIGHLIGHTS

- Novel microwave-assisted polyol synthesis of vanadium MOF materials introduced.
- Original nano-sheet and paperclip morphologies of V-MOF derived nanocomposites.
- VOx/Carbon and VOx/nitrogen-doped carbon successfully utilized in Na-ion batteries.
- Improved electrochemical behavior of VOx/N-doped carbon due to nitrogen doping.
- Low irreversible capacity and high performance V-MOF derived nanocomposites observed.

GRAPHICAL ABSTRACT

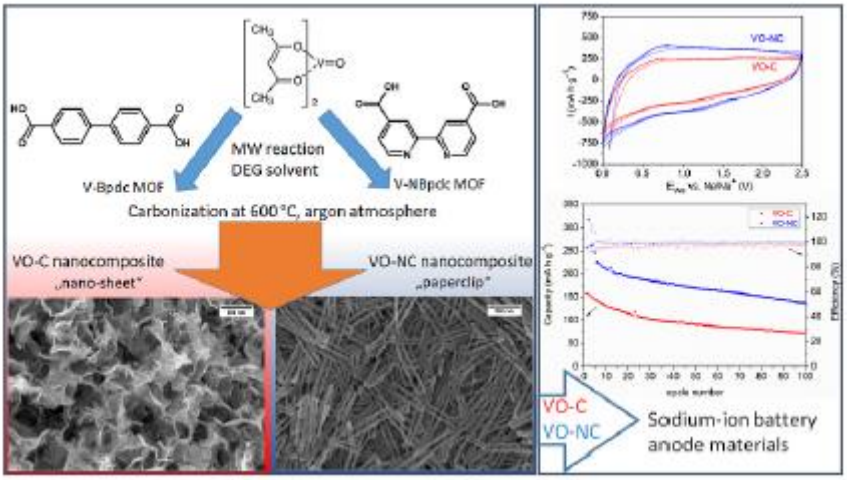

ABSTRACT

In this work, vanadium metal-organic framework derived VOx/carbon and VOx/N-doped carbon nanocomposites are presented. The methodology introduced here is based on a novel polyol synthesis of vanadium metal-organic frameworks (MOFs) involving a microwave-assisted solvothermal reaction of vanadyl acetylacetonate with biphenyl-4,4'-dicarboxylic acid (Bpdc) and/or 2,2'-bipyridine-4,4'-dicarboxylic acid (NBpdc) in diethylene glycol (DEG) at the temperature of 230 0C. The V-based MOFs, labeled as V-Bpdc and V-NBpdc, were used as precursors for the preparation of VO_x/carbon and VO_x/N-doped carbon nanocomposites with unique sponge-like nano-sheet and paperclip-like morphology, respectively. The nanocomposites were obtained via thermal transformation of as-prepared vanadium MOFs in the argon atmosphere at 600 0C. The VO_x/carbon sample consists of nano-sheets with the thickness 5-20 nm while the VO_x/N-doped carbon paperclip-like nanocomposite has a rod diameter 35-70 nm. It was found that the approach reported here provides an effective and simple preparation pathway of carbon-based nanocomposites containing homogeneously distributed VO_x species. Both V-MOFs and V-MOF-derived nanocomposites were characterized by the variety of physicochemical methods. In the following step, the obtained nanocomposites were investigated as electrode materials in sodium-ion batteries. Based on the obtained results, high electrochemical activities of VO_x/carbon and VOx/N-doped carbon nanocomposites were evidenced. Particularly, in the case of VO_x/N-doped carbon-based electrode, high capacity and low irreversible capacity were achieved. Therefore, reported materials are found to be promising candidates for electrode materials in sodium-ion batteries.

Keywords: Vanadium, Metal-organic framework, Carbon, Nanocomposites, Sodium-ion batteries

1. Introduction

Nowadays, sodium-ion batteries (SIBs) are considered highly promising post-lithium power sources **[1,2]**. Considering the advantages of SIBs mainly linked to the large-scale energy storage and conversion due to the high abundance and the low cost of sodium compared to lithium, SIBs have attracted growing attention in the field of energy storage. However, some limitations, such as the relatively lower ionization potential of Na+ ion in comparison to lithium-ion batteries (LIBs) and a bigger diameter of Na+ ions, which confines the diffusion, still restrict final applications of SIBs. Moreover, the bigger diameter of the Na+ ion causes a decomposition of the graphite anode structure. Thus, graphite as anode for Na-ion batteries is unsuitable and the development of new stable anode materials has been required **[3]**. These drawbacks mentioned above have led to lower energy density and poor electrochemical performance in comparison with LIBs **[4]**. Hence, many strategies involving the preparation of nano-sized composite materials have been applied as promising solutions for SIBs performance improvement **[4]**. Nevertheless, the research, development, and application of new composite electrode materials suitable for SIBs are still the challenge.

The composite materials based on a carbon matrix have gained an immense research interest due to their high surface area, thermal, and electrochemical features, hence, these materials are promising candidates for application in electrochemical power sources **[5-7]**. As has been reported, carbon-based materials can be used as negative electrode materials in SIBs **[1,2,4,8-10]**. However, it has to be taken into account that materials with a high graphitization degree (such as graphite) exhibit unfeasible capacity (less than 100 mAh g^{-1}) for Na^+ storage **[11]**. In response to the limitation mentioned above, the attention of ongoing research has been focused on disordered soft and hard carbon-based materials **[12]**. Also, advanced and hierarchical nanocomposites have been studied as promising candidates for SIB electrodes **[13-15]**. On one hand, these materials possess high reversible capacity

during the long-term cycling, but on the other hand, they have high irreversible capacity in the first cycles **[13,16-19]**.

It has been demonstrated that due to the high abundance, low cost, and high theoretical capacities of vanadium oxides (VO_x), carbon-based composites containing vanadium oxide are promising materials for electrochemical devices such as supercapacitors, lithium-ion, and/or sodium-ion batteries **[20-23]**. For example, VO/VO_x/carbon nanofiber composite and hierarchical porous VO_x@carbon composite have been applied as electrodes for supercapacitors **[24,25]**. Recently, rGO decorated vanadium pentoxide has been proposed as a supercapacitor electrode material **[26]**. Dandelion-like V_2O_3/C composite and urchin-like V_2O_3/C hollow nanospheres obtained from hydrothermal reactions have been used as anode material for lithium-ion batteries **[27,28]**. Moreover, as it has been reported recently, nitrogen doping is found as an additional improvement of the carbon matrix in terms of its electrochemical activity and conductivity **[29]**. For example, an N-doped carbon/oxygen-deficient vanadium oxides heterostructure composite prepared from vanadyl glycolate precursor has been used as anode for SIBs **[30]**. As has been proposed in the work by Ren et al., it is suggested that VO and V_2O_3 can convert into Na_2O and V species according to the following reaction equations: $VO + 2e^- + 2Na^+ \rightarrow Na_2O + V$ and $V_2O_3 + 6e^- + 6Na^+ \rightarrow 3Na_2O + 2V$ upon charging/discharging process, respectively [30]. Zhang et al. have demonstrated preparation of amorphous vanadium oxide/MXene nanohybrid and its application in SIBs **[31]**. Other recent work by Liu et al. has described SIB electrode based on amorphous vanadium oxide integrated in carbon nanofibers **[32]**. Furthermore, it has already been reported that amorphous VO_x exhibited better properties for Na^+ storage that the crystalline V_2O_5 phase **[33]**.

Considering the application in energy storage devices, the homogeneity of vanadium-carbon composites is found to be a decisive property of the final material. Currently, a decomposition of metal-organic frameworks has been proposed as an effective pathway for the preparation of homogeneous carbon-based composites **[34-38]**. The controlled morphology of MOFs has also led to advanced architectures of MOF-derived composites **[39]**. The MOFs have been defined as crystalline solids constructed from metal ions or metal-oxo clusters cross-linked with an organic linker **[40]**. The diversity of carbon-containing linkers with adjustable size, connectivity, and functional groups enables the tuning of the final properties of MOFs such as their composition, architecture, porosity, and electrochemical properties **[41-47]**. The conventional preparation procedures of MOFs usually involve solvothermal reactions of a metal salt or metal-oxo clusters with multifunctional carboxylate linkers in N,N'-dimethylformamide **[42, 48]**. It is worth noting that microwave-assisted syntheses of MOFs have gained a growing attention because they provide significant enhancement of the reaction rates and the ability to control the phase and size of products **[37,49,50]**. In particular, the vanadium MOFs with MIL-47 and MOF-48 architectures, as reported by the group of Yaghi, have featured chemical stability and high catalytic activity in the conversion of methane to acetic acid **[51].** MOF structures of Vanadium with 1,4-ben-zenedicarboxylate (bdc) linker have been reported by Wang et al. **[52]** and Kaveevivitchai et al. **[53]**. Noteworthy, the VIV(O)(bdc) (MIL-47) has been used as the cathode material for lithium-ion battery systems **[53]** or electrode material for supercapacitors **[54]**. A more comprehensive review on the syntheses and applications of vanadium MOFs has been published by the group of Van der Voort **[55]**.

Recently, it has been demonstrated that research on vanadium MOF-derived composites gained a considerable attention in the field of electrochemistry and energy storage. For example, vanadium MIL-88B MOF-derived porous shuttle-like vanadium oxides for sodium-ion battery applications have been described by Cai et al. **[56]**. Recently, N-doped porous carbon nanorods decorated with ultra-small V_2O_3 for sodium-ion capacitors have been obtained from naphthalene dicarboxylate based

vanadium MOF **[57]**. Moreover, vanadium benzenedicarboxylate MOF derived porous V_2O_5 plates have been applied in an aqueous zinc ion battery **[58]**. Further, MIL-47(V) MOF-derived hierarchical lasagna-structured V_2O_3@C has been studied as a sulfur host for lithium-sulfur batteries. Considering the final application of MOFs and MOF-derived composites, it can be argued that control of their morphology influences their final performance **[39,59]**. Based on the survey mentioned above, it can be concluded, that advanced composite materials derived from MOFs have brought the advantages of high homogeneity and simplicity of one-pot synthetic methodology **[60,61]**.

Herein we present facile microwave-assisted polyol synthesis of vanadium-based metal-organic framework materials. The presented methodology is based on the reaction of vanadyl acetylacetonate precursor with biphenyl-4,4'-dicarboxylic and 2,2'-bipyridine-4,4'-dicar-boxylic acid linkers in diethylene glycol solvent. As demonstrated in this work, our approach leads to the specific morphology of MOF products. Prepared vanadium MOFs were used as precursors for the preparation of VO_x/carbon and VO_x/N-doped carbon composites. Note, we observed sponge-like nano-sheet morphology of VO_x/carbon nanocomposite and the unique paperclip-like morphology in case VO_x/N-doped carbon composite. Electrochemical properties of carbon-based nanocomposites were studied to investigate their potential for an application in electrochemical devices such as SIBs or supercapacitors.

2. Experimental

2.1. Chemicals

Vanadyl acetylacetonate VO(Acac)2 (99%, M_w = 265.157 g mol^{-1}) was purchased from Acros Organics. Biphenyl-4,4'-dicarboxylic acid (H2bpdc, 97%, M_w = 242.23 g mol^{-1}), and 2,2'-bipyridine-4,4'-dicar-boxylic acid (98%, M_w = 244.20 g mol^{-1}) were supplied from Sigma Aldrich. Diethylene glycol DEG (p.a.) and methanol (p.a.) were purchased from Penta (Czech Republic). Chemicals for Na-ion cell fabrication such as sodium perchlorate ($NaClO_4$), poly(vinylidenefluoride) (PVDF), N-methyl-2-pyrrolidone (NMP), ethylene carbonate (EC), and dimethyl carbonate (DMC) were supplied from Sigma Aldrich. Super P carbon was obtained from TIMCAL.

2.2. Synthesis of V-Bpdc material

The typical synthesis of V-Bpdc material in a microwave reactor was performed as follows: VO(Acac)2 (0.506 g, 1.90 mmol) was dispersed in 60 ml of diethylene glycol (DEG) in a Teflon reaction vessel under an ambient atmosphere. Then, biphenyl-4,4'-dicarboxylic acid (0.463 g, 1.91 mmol), labeled as Bpdc, was added and the vessel was tightly closed and placed into a microwave reactor. The reaction mixture was heated up to 230 °C under microwave irradiation. Microwave power was set to 100% (600 W). The reaction was stopped after 30 min. The microwave reactor record is illustrated in Supplementary materials (Fig. 1(S)). Once the reaction mixture was cooled to 50 °C, the reactor was removed and the resulting green-brown precipitate was separated by centrifugation and washed with methanol. The powder product was dried at 90 °C in an oven and weighed.

2.2.1. The analysis of V-Bpdc powder product

FTIR (ATR, diamond crystal, cm^{-1}) ν: 452 vs (V-O), 505 s, 537 m (δ CC, bending), 551 m, 600 w, 686 s (ring out-of-plane), 705 vw, 756 m (ring out-of-plane), 766 s (δ CH, bending), 793 vw, 846 m (δ CH),

879 m (δ CH), 909 m (δ CH, bending), 1009 w (v V-O), 1077 m (δ CH_3), 1122 w (δ CH_3), 1147 w, 1182 w, 1246 vw (v CC), 1291 w, 1378 m (vsym COO), 1409 vs (v_{sym} COO), 1524 vs (v_{asym} COO), 1572 m (v_{asym} COO), 1608 w, 1686 m (v C=O), 2863 vw, 2924 vw (v CH_3).

Elemental analysis: (ICP-OES): 16.34 ± 0.05 wt% of vanadium.

The synthetic procedure of V-NBpdc material was performed in the same manner as in the case of V-Bpdc product, however, the 2,2'-bipyridine-4,4'-dicarboxylic acid (0.468 g, 1.92 mmol), labeled as NBpdc, was used as an organic linker (**Fig. 2(S)**).

2.2.2. The analysis of V-NBpdc powder product

FTIR (ATR, diamond crystal, cm^{-1}) v: 419 w, 482 w (V-O), 592 w, 669 w, 697 vs (ring out-of-plane), 724 m (ring out-of-plane), 777 s (δ CH, bending), 875 m (v_{sym} CN), 911 w, 973 s, 1029 w (v CC/δ CH), 1066 m (δ CH), 1123 m (δ CH), 1234 m (v_{asym} CN), 1264 w, 1288 m (v CN), 1354 s (v_{sym} COO), 1401 vs (v_{sym} COO), 1486 vw (v CN/δ CH_3), 1554 m (v_{asym} COO), 1616 m (v_{asym} COO), 1728 m (v C=O), 2869 vw, 2927 vw (v CH_3), 3078 vw (v CH), 3422 vw (v OH).

Elemental analysis: (ICP-OES): 14.27 ± 0.09 wt% of vanadium.

The carbonization process of V-Bpdc and V-NBpdc MOF products was carried out in a tubular furnace under an inert atmosphere of argon at the temperature of 600 °C for 3 h. The heating up to 600 °C was set with rate 5 °C min^{-1}. The carbonized products obtained by heat treatment of V-Bpdc and V-NBpdc MOFs were labeled as VO-C and VO-NC, respectively.

2.3. Electrochemical analysis and electrode preparation

A mixture consisting of the active mass (VO-C or VO-NC sample), PVDF (binder), and Super P carbon was mixed by a magnetic stirrer in a vial with 1.5 ml NMP (N-methyl-2-pyrrolidone) in the weight ratio as follows: active material (VO-C or VO-NC) 80%, Super P 10%, PVDF 10%. The resulting mixture was deposited on an Al foil by a 200 |im coating bar, dried at 60 °C under ambient atmosphere, and, after the solvent was evaporated, pressed with the pressure of 300 kg cm^{-2}. The discs with a diameter of 18 mm were cut out from the coated Al foil and subsequently dried at 110 °C under the vacuum. The loading of the active mass of the electrodes was 2.7 ± 0.1 mg cm^{-2}. Finally, the discs were inserted into an electrochemical cell El-Cell© ECC-Std and assembled in the argon atmosphere inside a Jacomex glove box with less than 1 ppm of oxygen and water content. A sodium metal disc was used as the anode and 1 mol l^{-1} NaClO4 in EC:DMC in the ratio 1:1 w/w as the electrolyte. The electrolyte was soaked into the glass fiber separator. Cyclic voltammetry (CV), electrochemical impedance spectroscopy (EIS), and galvanostatic cycling were used for electrochemical characterization. All methods were performed on the VMP3 potentiostat (BioLogic). CV was done in the potential window from 0.01 to 2.5 V vs. Na/ Na^+ and scan rate were set to 0.5, 1, 5, and 10 mV s^{-1}. Galvanostatic cycling was carried out within a potential window from 0.01 to 2.5 V vs. Na/Na^+. Long-term cycling at 0.2C for 100 cycles was tested for both materials. The second test was cycling at different C-rate from 0.1C up to 5C. The first step was performed as follows: 20 cycles at 0.2C, then 5 cycles at 0.5C, 1C, and finally at 2C. Subsequently, the C-rate was decreased by the same step to 0.2C with 5 cycles at every C-rate (1C, 0.5C, 0.2C). EIS was performed in a frequency range from 1 MHz to 0.1 Hz, with an amplitude of 10 mV.

2.4. Instrumentation and characterization methods

2.4.1. Microwave-assisted synthesis

The V-Bpdc and V-NBpdc materials were synthesized under an ambient atmosphere in a PTFE-lined microwave reactor ERTEC Magnum II (600 W; 2.45 GHz). Microwave power was set to 100% (600 W) and the reaction mixture was heated up to 230 ° C. The reaction duration was 30 min.

2.4.2. Chemical/elemental analyses

The GC-MS measurement of reaction byproducts was performed on an ISQ QD single quadrupole mass spectrometer coupled with a Trace 1300 gas chromatograph by Thermo Scientific. The gas chromatograph was equipped with a Rxi-5ms column (30 m, 0.25 mm, film thickness 0.25 im) and the temperature program was used as follows: 80 °C-240 °C with the ramp 10 °C min^{-1}, held at 240 °C for 1 min. Split injection mode (60 ml min^{-1}, split ratio 60) was used with the inlet temperature of 280 °C, transfer line, and EI source 220 °C (ionization energy: 70 eV, emission current: 30 μA). Vanadium contents in V-Bpdc and V-NBpdc materials were determined by ICP-OES spectroscopy performed on an iCAP 6500 (Thermo, GB) spectrometer (vanadium spectral lines λ = 309.311 and 292.402 nm).

2.4.3. Structural characterizations

The powder XRD patterns were recorded on a Rigaku MiniFlex 600 diffractometer equipped with a CoK_α (λ = 1.7903 Å) X-ray tube (40 kV, 15 mA). Data processing was done with Rigaku PDXL2 software. Powder XRD diffractograms of electrode materials after charge/discharge cycling were carried out on a Rigaku Miniflex 600 equipped with CuK_α (λ= 1.5406 Å) X-Ray tube (40 kV 15 mA). The electrode material samples on the aluminum collector were placed on Si wafer substrate and put into a custom-made cell for post-mortem measurements underan inert argon atmosphere **[62]**. Due to the overloading of the detector caused by strong reflections of the silicon wafer, the silicon diffraction in the range 28-29° two theta was measured separately.

2.4.4. Infrared and Raman spectroscopy

The FTIR spectra were recorded on a Thermo Nicolet 6700 spectrometer using an ATR technique with the diamond crystal (resolution 2 cm^{-1} 400-4000 cm^{-1}). Raman spectroscopy was performed on a Thermo Raman microscope Nicolet DXR equipped with a He-Ne laser with emission wavelength 633 nm (power 1 and 4 mW). The spectra were recorded from 50 to 2000 cm^{-1}.

2.4.5. X-ray photoelectron spectroscopy

X-ray photoelectron spectroscopy measurements were carried out on a Kratos Analytical Axis Supra spectrometer equipped with mono-chromatized Al-Kα radiation (1486 eV). The sample powders, pressed in small stainless troughs of 4 mm diameter, were placed on an insulating home-made ceramic carousel. The pressure in the analysis chamber was around 10^{-6} Pa. The analyzed area was approximately 1.4 mm^2 and the pass energy was set at 150 eV. The C 1s peak of carbon has been fixed to 284.8 eV to set the binding energy scale **[63,64]**. Data treatment was performed with the CasaXPS program (Casa Software Ltd, UK) and some spectra were decomposed with the least-squares fitting

routine provided by the software with a Gaussian/Lorentzian (85/15) product function and after subtraction of a nonlinear baseline.

2.4.6. Thermal analysis and heat treatment

Thermogravimetric analyses were performed on a Setaram LabSys Evo instrument with TG/DSC sensor in the air atmosphere (heating rate 5 °C min^{-1}, up to 600 °C, airflow 60 ml min^{-1}) and helium (5 °C min^{-1}, up to 600 °C, 60 ml min^{-1}). Dried powders were heated in a Nabertherm LE 4/11/R6 tubular furnace at 600 °C (5 °C min^{-1}) for 3 h in the argon atmosphere.

2.4.7. Microscopy

The scanning electron microscopy (SEM) was obtained with a SEM Nova NanoSEM (FEI) operated at 5 kV and equipped with Schottky field emission gun (FEG) electron source and TLD secondary-electron detector. The SEM energy dispersive X-ray (EDX) analysis was performed with EDX spectrometer Octane Plus (EDAX, AMETEK, Inc) with a SDD detector. The transmission electron microscopy was performed with a high-resolution TEM (HRTEM) Titan Themis 60-300 High Base (Thermo Fisher Scientific) operated at 300 kV and equipped with a highbrightness X-FEG electron source and a spherical aberration image (C_s)-corrector. The scanning TEM EDX (STEM-EDX) analysis was performed with Super-X spectrometer (Thermo Fisher Scientific) with four 30 mm2 windowless detectors. The STEM imaging was performed with high-angular annular dark-field (HAADF) detector (Fishione) providing atomic Z-contrast. The sample for TEM was dispersed in methanol and 4 |il of this suspension were placed on a QuantiFoil R 2/1 300 mesh copper grid and dried spontaneously by evaporation at the ambient temperature. SEM images of electrode materials before and after charge/ discharge cycling were recorded on a TESCAN VEGA3 XMU electron microscope.

2.4.8. Nitrogen adsorption/desorption

Nitrogen adsorption/desorption isotherms were collected at the temperature of 77 K on a BELsorp Mini II (Japan). Before measurement, the samples were degassed in the BELsorp preparation unit at 100 °C for 19 h. Surface areas (SA) and total pore volumes (V_{tot} at p/p_0 = 0.99) were determined by volumetric techniques **[65,66]**. The specific surface area was calculated from the multipoint Brunauer-Emmet-Teller (BET) method using at least five data points with relative pressures between 0.05 and 0.30 **[65]**.

3. Results and discussion

3.1. Synthesis and materials characterization

Vanadium-based metal-organic frameworks were prepared via microwave-assisted polyol solvothermal method from vanadyl acetyla-cetonate in diethylene glycol (DEG) at 230 °C **(Fig. 1)**. As organic linkers, biphenyl-4,4'-dicarboxylic (labeled as Bpdc) and 2,2' -bipyr-idine-4,4'-dicarboxylic acid (labeled as NBpdc) were used **(Table 1)**. A nitrogen-containing linker was employed for further nitrogen doping of the carbon matrix of VO_x/carbon composite obtained by the carbonization of vanadium MOF. The microwave-assisted approach enables rapid and direct heating of the reaction mixture and the required reaction temperature is reached in a short time in contrast with conventional heating

methods. It is worth mentioning that V-MOF products were obtained after 30 min of MW-assisted reaction. Due to the strong interaction of molecule dipoles with microwaves, it can be expected that the reaction kinetics in the presented system is increased **[67]**. Moreover, Yang and co-workers have considered that the ordered high-frequency vibrations introduced by MW irradiation may lead to specific or/and different morphologies than those obtained via conventional heating **[68]**. Contrary to conventional MOF preparation methods involving solvothermal reactions in N,N'-dimethylformamide **[42,48]**, the polyol MW-assisted approach reported here provided different and novel MOF architectures.

MW-assisted reaction byproducts were determined by the GC-MS technique **(Fig. 2)**. The solution separated after reaction mixture centrifugation was injected into the GC-MS instrument. In the chromatogram **(Fig. 2)**, the presence of acetone, 2-(2-hydroxyethoxy)ethyl acetate, and 2-[2-[2-(2-hydroxyethoxy)ethoxy]ethoxy]ethyl acetate was confirmed. These products are formed from acetylacetonate precursor after its decomposition during the MW reaction. It can be argued that the acetylacetonate group is decomposed into two fragments represented by the acetyl group and enol-like intermediate **[69]**. Further, it is proposed that (2-(2-hydroxyethoxy)ethyl acetate) ester and acetone are formed from the reaction of acetyl group and enol-like intermediate with DEG solvent.

As-prepared vanadium MOF products were analyzed by infrared spectroscopy. FTIR spectra of V-Bpdc and V-NBpdc samples are depicted in **Fig. 3(a)**. Intense absorption bands raised at 1409 and 1402 cm^{-1} are attributed to υ_{sym} modes of carboxylate groups. The vibrational bands located in region 1525-1617 cm^{-1} are ascribed to υ_{asym} vibrations of carboxylate groups. The vibrational bands related to aromatic ring out-of-plane and C-H vibrations of the linker are found in the wavenumber region 670-790 cm^{-1} **[70]**. Vanadyl group (V=O) in the V-Bpdc sample can be assigned to a vibrational band with wavenumber 1012 cm^{-1} **(Fig. 3)**. Noteworthy, an interaction between nitrogen atoms in the NBpdc linker and vanadyl group may be proposed from the shift of V=O absorption band in the FTIR spectrum of V-NBpdc sample at 974 cm^{-1} **[71]**. This shift is due to a coordinate bond formed between the lone pair of electrons on pyridinic nitrogen and the empty d-orbital of the vanadium, which results in an increase of electron density around the vanadium and repulsion of the V=O bond **[72,73]**. The FTIR spectra of vanadium precursor, biphenyl-4,4'-dicarboxylic, and 2,2'-bipyridine-4, 4'-dicarboxylic acid linkers, as well as the spectra of V-MOF products, are compared in the **supplementary information (Fig. 3(S))**. X-ray powder diffraction was employed for the investigation of the crystallinity of prepared vanadium MOF materials. As illustrated in **Fig. 3(b)**, the diffractogram of V-Bpdc exhibits broad diffractions in the range 5-15° and at 27° two theta degrees. Sharp diffraction is recorded at 20° two theta degrees. Based on the diffractogram it can be concluded that the V-Bpdc structure exhibits low crystallinity. For comparison, dif-fractograms of $VO(Acac)_2$ and organic linkers are depicted in the supplementary information **(Fig. 4(S))**. Powder XRD diffractogram of V-NBpdc MOF product shows broad diffraction patterns indicating the amorphous character of this product. The amorphous character can be considered as a result of a lack of long-range periodic order, while the basic building blocks and connectivity found in common crystalline MOF structures are retained [74]. Further, the low crystallinity and amorphous character of products are proposed to be a consequence of reaction procedure and fast MW-assisted heating.

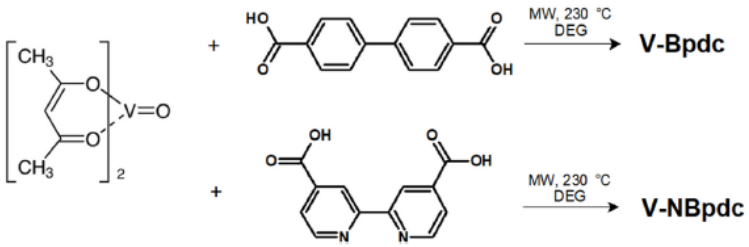

Fig. 1. Reaction procedure scheme.

Table 1 Reaction precursor amounts and yields of the products.

sample	m V [g]	n V [mmol]	linker	m [g]	n [mmol]	Yield [g]
V-Bpdc	0.506	1.90	Bpdc	0.463	1.91	0.568
V-NBpdc	0.503	1.89	NBpdc	0.468	1.92	0.545

The thermal behavior of prepared V-MOF materials was studied in atmospheres of air and helium up to 600 °C. Thermogravimetric curves recorded in the air are displayed in **Fig. 4.** It can be concluded that the TG curves of both V-Bpdc and V-NBpdc samples reveal an almost similar shape with two distinct mass losses. The first mass loss (23.8% V-Bpdc; 21.8% V-NBpdc) between 140 and 260 °C is assigned to the release of residual DEG solvent. The second mass loss (42.0% V-Bpdc; 45.7% V-NBpdc) observed in the temperature range 290-400 °C is ascribed to the oxidation of linker molecules. The residual mass of the V-Bpdc and V-NBpdc samples after TG analysis in the air was 28.2 and 25.5%, respectively. Based on the powder XRD technique, the residues after TG analysis in air correspond to the crystalline phase of V_2O_5 **(Fig. 5(S))**. Furthermore, it can be concluded, that the content of vanadium in the V-Bpdc and V-NBpdc sample is 15.8 and 14.3 wt%, respectively **(Table 2).** These values are in good agreement with the vanadium contents obtained from ICP-OES analysis **(Table 2)**. It can be mentioned that TG analysis performed in the helium atmosphere **(Fig. 4)** shows differences between V-Bpdc and V-NBpdc samples. As displayed, the TG curve of the V-Bpdc MOF sample reveals two separated mass losses (23.2 and 24.7%) in temperature ranges 220-380 °C and 410-550 °C connected with the release of DEG solvent and CO_2 from carboxylate groups of Bpdc linker, respectively **[75]**. In the case of the V-NBpdc sample, gradual mass loss consisting of at least three steps (140-250; 250-350; 350-550 °C) is recorded. The residual mass of the V-NBpdc sample after the TG analysis in the helium atmosphere was 46.5%. It can be agreed that individual mass losses on the TG curve of the V-NBpdc sample are not as significantly distinguished as in the case of the V-Bpdc sample. The differences between the TG curves of V-Bpdc and V-NBpdc samples recorded in helium can be addressed to the different thermal stability of the V-NBpdc sample in the helium atmosphere. Such behavior may be a result of a specific arrangement between vanadium species and the NBpdc linker.

Based on the data obtained from TG analyses in the air atmosphere, approximated formulas of vanadium MOF materials can be derived. Since the mass losses are related to DEG solvent and oxidation of linker, whereas the residual mass corresponds to V2O5, the approximated formula for V-Bpdc and V-NBpdc can be expressed as VO (Bpdc)0.66(DEG)0.72 and VO(NBpdc)0.77(DEG)0.73, respectively.

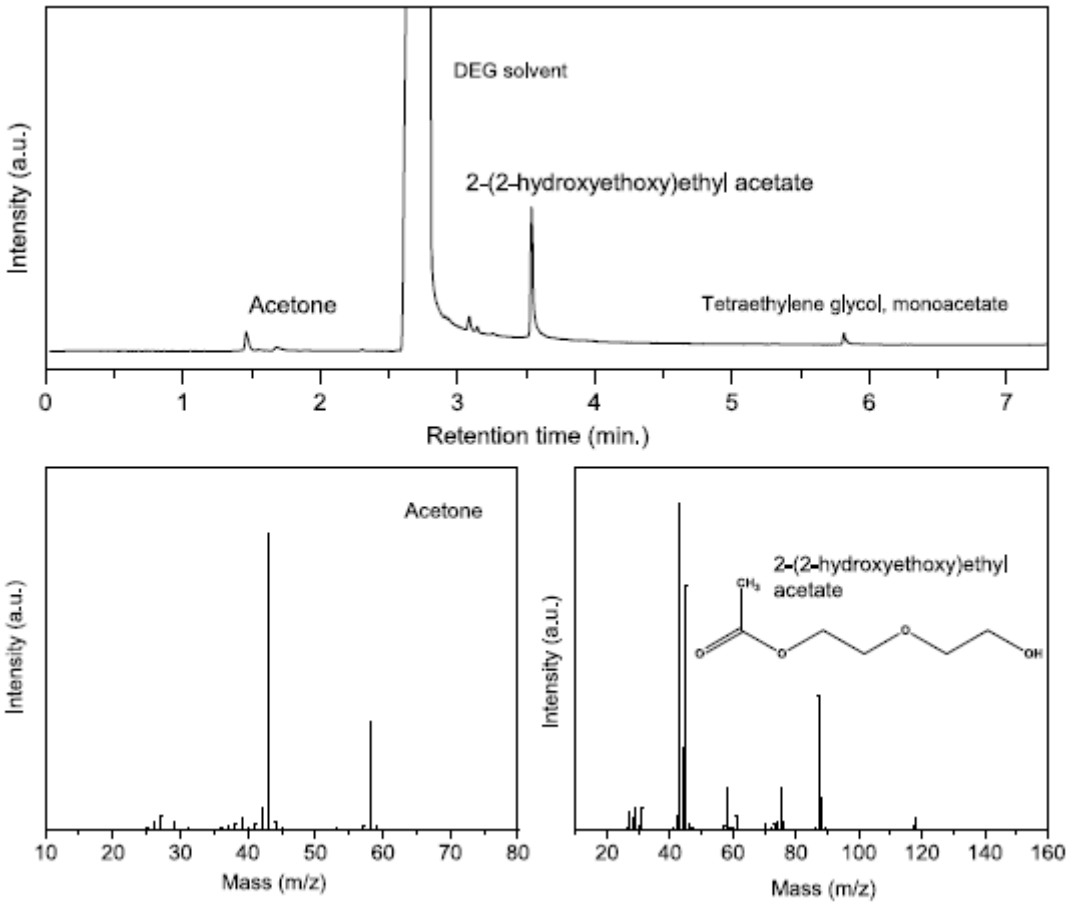

Fig. 2. GC chromatogram of the reaction mixture after product separation (upper). MS spectra of reaction byproducts.

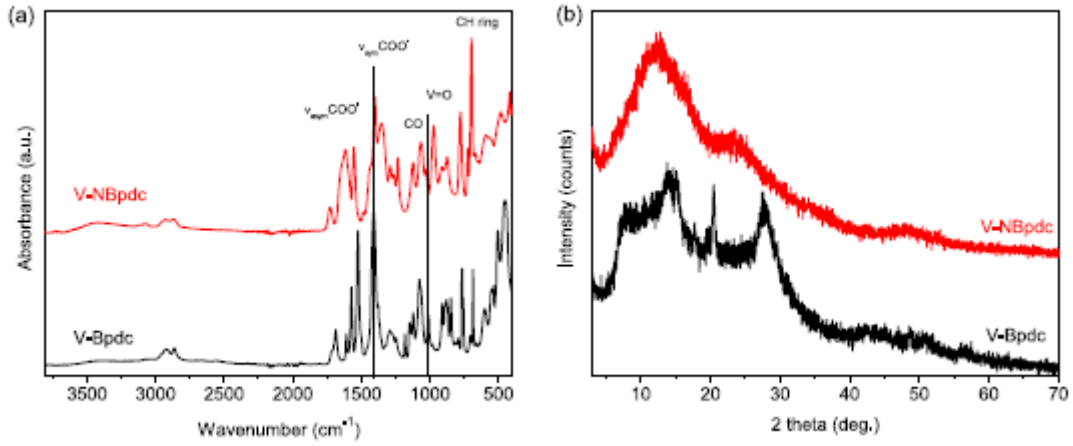

Fig. 3. (a) FTIR spectra of V-Bpdc and V-NBpdc MOF products. (b) Powder XRD pattern of V-Bpdc and V-NBpdc MOF products.

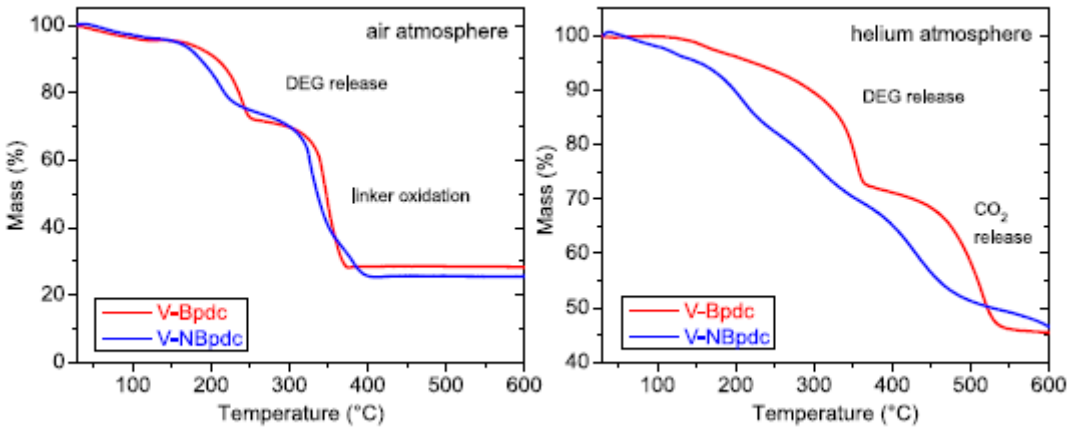

Fig. 4. TG curves of V-Bpdc and V-NBpdc MOF products performed in the air atmosphere (left) and helium atmosphere (right).

Table 2 Elemental composition values and TG residual masses.

MOF	V content wt%		TG Residual mass %		composite	EDX wt%			
sample	ICP	TG[a]	Air	He	sample	V	O	C	N
V-Bpdc	16.34 ± 0.05	15.8	28.2	45.4	VO-C	35.4	14.1	50.5	–
V-NBpdc	14.27 ± 0.09	14.3	25.5	46.5	VO-NC	30.4	12.5	46.0	11.1

[a] *determined from V_2O_5 residue after TG analysis in air.*

The elemental composition of VO-C and VO-NC nanocomposites was examined by the EDX technique **(Figs. 6(S) and 7S)**. The content of vanadium, oxygen, carbon, and nitrogen elements is listed in **Table 2.** As expected, both materials contain carbon as a major weight part. The VO-C nanocomposite contains 35.4 and 14.1 wt% of vanadium and oxygen, respectively. These numbers correspond to 12.1 at% of vanadium and 15.2 at% of oxygen. In the VO-NC sample, 30.4 and 12.5 wt% of vanadium and oxygen, respectively, were found **(Table 2)**. These contents correspond to 10.1 at% of vanadium and 13.1 at% of oxygen. Moreover, it is observed that nitrogen atoms from NBpdc linker are present in carbonized material in the content of 11 wt%. Therefore, the N-doped carbon-based composite has been obtained.

Carbonized samples labeled as VO-C and VO-NC derived from V- Bpdc and V-NBpdc MOF products, respectively, were characterized by powder XRD technique and Raman spectroscopy. Powder XRD diffractograms of both VO-C and VO-NC samples exhibited an amorphous character with no diffractions characteristic for any vanadium oxide crystalline phase **(Fig. 5(a))**. Nevertheless, it has already been reported, that even amorphous vanadium oxide can be used in electrochemical energy storage **[76]**. The Raman spectra depicted in **Fig. 5(b)** displayed two bands around 1340 and 1590 cm^{-1}, which are characteristic for vibrational modes of the disordered carbon (D-band) and in-plane vibrations (E_{2g}) of ordered graphitic carbon (G-band), respectively. It can be pointed out that the intensity, shape, and resolution of D and G bands recorded in the case of the VO-C sample is better than those of the VO-NC sample. On one hand, a more intense and narrow G-band suggests the formation of thin or a graphitic-like morphology in the case of the VO-C sample. On the other hand, weak, wide, and severely overlapped G and D bands are indicative of amorphous carbon structures in the case of VO-NC

material. This observation is proposed to be a consequence of VO-C sample morphology (discussed later).

An X-ray photoelectron spectroscopy (XPS) was employed to thoroughly investigate the bonding relations between elements in both as-prepared MOF materials (V-Bpdc, V-NBpdc) and carbonized samples (VO-C, VO-NC). Survey scans over the whole binding energy region are given in **supplementary information (Figs. 8(S)-11S)**. XPS spectra of the V-Bpdc MOF sample are shown in **Fig. 6.** C 1s XPS spectrum of V-Bpdc sample (**Fig. 6** upper left) exhibited three signals with the binding energies 284.7, 286.2, and 289.0 eV which are assigned to C-(C,H) of the aromatic rings, C-O^- groups, and to O=C-O^- carboxylate groups, respectively.

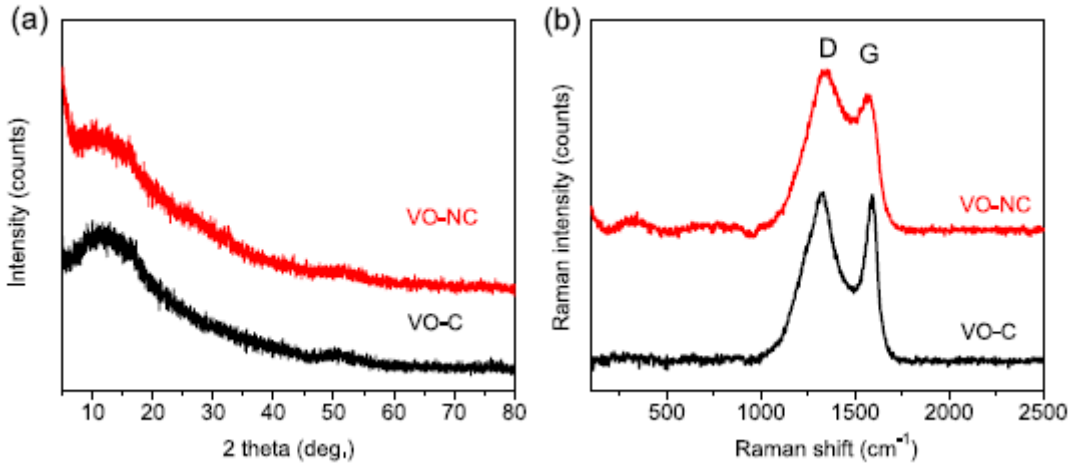

Fig. 5. (a) Powder XRD patterns of MOF derived composites VO-C and VO-NC. (b) Raman spectra of VO-C and VO-NC composites.

These species are attributed to Bpdc linker. O 1s spectrum of V-Bpdc (**Fig. 6** upper right) revealed three contributions with binding energies 530.7, 532.0, and 533.1 eV. The O 1s peak exhibited its major part at 532.0 eV and this contribution can be ascribed to carboxylate oxygen atoms (O=C-O^-) with bidentate coordination to vanadium atoms. The minor O 1s part, in the higher BE side (533.1 eV), can be understood as a residue of the unreacted acidic form of the Bpdc and/or from other -OH groups that could be associated with DEG solvent residue. The component detected at binding energy 530.7 eV is assigned to V-O groups. V 2p XPS spectrum of V-Bpdc sample displayed in **Fig. 6** (upper, right) contains V $2p_{3/2}$ components detected at 516.7, and 517.8 eV. V $2p_{1/2}$ components are found at binding energies of 523.9 and 525.1 eV. According to reported values for V $2p_{3/2}$ species, the peak at 517.8 eV is assigned to the V^{5+} oxidation state and the peak with binding energy 516.7 eV is indicative of the V^{4+} oxidation state **[77,78]**. XPS spectra of carbonized sample VO-C are shown in **Fig. 6** at the bottom. As displayed in the C 1s spectrum, major contribution assigned to graphitic C-(C,H) groups is detected at BE 284.4 eV. In particular, the asymmetry of the main component in the high BE side could be understood as the simultaneous presence of oxidized carbon species and graphitic-like compounds, this latter presenting intrinsic asymmetry of the C 1s peak. Further, the C 1s shoulder component with BE 283.3 eV could be associated with the V-C bond **[79]**. The bottom part of **Fig. 6** illustrates O 1s and V 2p XPS spectra of VO-C nanocomposite. The peak detected at 530.8 eV is indicative for V-O species, whereas the shoulder contribution at the higher BE side is assigned to residual C-O species preserved after carbonization. The detection of a broad component in the high BE side of the O 1s peak could be

associated with the presence of oxidized carbon species. In the case of the V 2p XPS spectrum of the VO-C sample, the V $2p_{1/2}$ components are found at binding energies of 523.1, 523.9, and 525.0 eV.

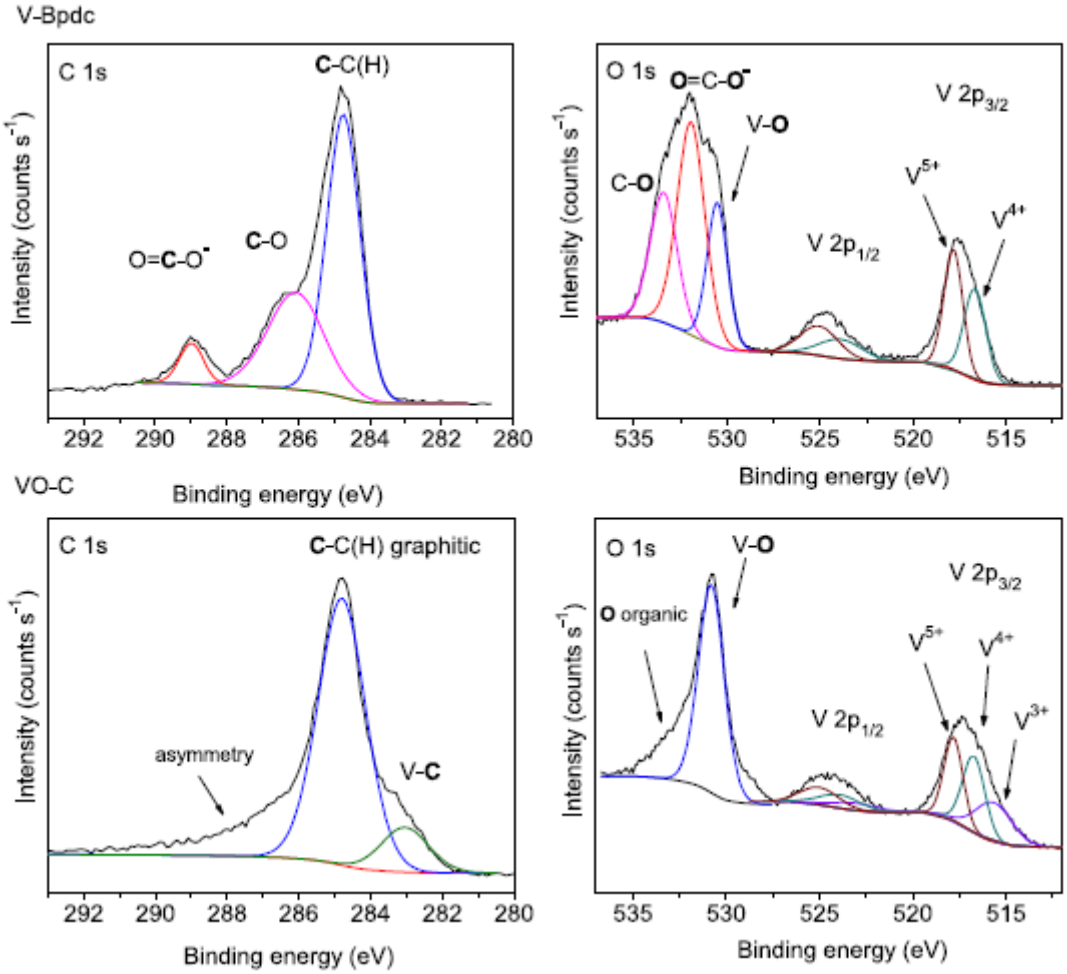

Fig. 6. XPS spectra of V-Bpdc MOF product (upper) and XPS spectra of MOF derived VO-C composite (bottom).

Based on the position of V $2p_{3/2}$ peaks with BE 516.7 and 517.8 eV raised from deconvolution of the recorded signal, one can argue that the vanadium element in the VO-C sample is presented in the V^{4+} and V^{5+} oxidation state, respectively **[77,78]**. The V $2p_{3/2}$ peak with BE of 515.7 eV can be assigned to the V^{3+} oxidation state **[78]**. The presence of V^{3+} states can be understood to be a result of V^{4+} reduction within the carbonization process.

XPS spectra of V-NBpdc and VO-NC samples are depicted in **Fig. 7, 10S, and 11S**. The C 1s XPS spectrum of the V-NBpdc sample (**Fig. 7**, upper) exhibited three contributions, and similarly as in the case of sample V-NBpdc these signals are ascribed to C-(C,H) of the aromatic rings, C-O^- groups, and O=C-O^- carboxylate groups. The bonding relation between carbon and nitrogen in the C 1s XPS spectrum is overlapped with broad C-(C,H) and C-O signals. As reported, the C-N bond produces an upshift to binding energy values between 285 and 287 eV, which is in the region of C-(C,H) species **[80]**. In the O 1s spectrum, two contributions with binding energies 531.7 and 533.0 eV were recorded. In this case, the peak at 531.7 eV can be associated with O=C-O^- groups coordinated to vanadium. The contribution with BE of 533.0 eV corresponds to C-O^- of unreacted NBpdc linker residue and/or other -OH groups

that could be associated with a residue of DEG solvent. V 2p spectrum of V-NBpdc sample displayed at the upper part of **Fig. 7** contains components detected at 523.6 and 524.8 eV that are assigned to the V $2p_{1/2}$ species. The V $2p_{3/2}$ contributions with binding energies 516.3 and 517.3 eV are indicative of V^{4+} and V^{5+} oxidation states, respectively **[31,77,78]**. As illustrated in **Fig. 7**, the V^{4+} state represents the major part of V 2p species in the V-NBpdc sample, which may originate from the possible coordination of nitrogen atoms contained in the NBpdc linker to vanadium **[81,82]**. The N 1s XPS spectrum of V-NBpdc MOF material shows a signal with BE 399.7 eV which can be attributed to pyrrolic nitrogen atoms **[83,84]**. In the C 1s XPS spectrum of sample VO-NC (**Fig. 7**, bottom), contributions of sp^2 C=C and sp^3 C-C (284.7 eV) graphitic species are found. The C-O^- and to O=C-O^- moieties are also present due to an incomplete removal during heat treatment. These groups are observed in the O 1s spectrum of the VO-NC sample as well **(Fig. 7)**, located in region 532-535 eV. The peak with BE 530.4 eV is indicative of V-O species. The V 2p spectrum of VO-NC contains V $2p_{1/2}$ contributions detected at 523.6 and 524.9 eV. The V $2p_{3/2}$ components with binding energies of 516.3 and 517.4 eV are characteristic for V^{4+} and V^{5+} valence, respectively **[77,78]**. It can be concluded that in the case of the VO-NC sample, the major contribution of V^{5+} oxidation state species is presented **(Fig. 7)**. Nitrogen incorporation is further evidenced in the N 1s XPS spectrum. As displayed in **Fig. 7** at the bottom, after the heat treatment of the V-NBpdc sample, different nitrogen species were detected in the spectrum. These components correspond to pyridinic-N (398.8 eV), pyrrolic-N (400.2 eV), and graphitic-N (401.6 eV), respectively **[83,84]**. Moreover, the V-N bond with the contribution at BE 396.8 eV was observed **[83]**. The presence of the V-N bond after carbonization can be understood as a consequence of nitrogen coordination to vanadium in parent V-NBpdc MOF **[81,82]**.

The morphology of V-MOF samples and carbonized products was studied by SEM microscopy. The images of as-prepared V-Bpdc and V-NBpdc samples are given in **supplementary information (Figs. 12(S) and 13S)**. SEM images of the vanadium MOF-derived carbon-based composites are displayed in **Fig. 8.** As can be seen, the sponge-like morphology with the nano-sheet architecture of particles **(Fig. 8(a))** was revealed in the image of the VO-C sample. Based on the SEM analysis, the thickness of nano-sheets is in the range of 5-20 nm. As a consequence of this architecture, the high intensity and narrow shape of the G band in the Raman spectrum were observed. The VO-NC composite exhibited unique "paperclip" morphology **(Fig. 8(b))** with the rod diameter ranging from 35 to 70 nm. This interesting architecture can be proposed as a result of the molecular geometry of V-NBpdc MOF formed from vanadium ions and 2,2'-bipyridine-5,5'-dicarboxylate linker during the solvothermal reaction. In addition, it can be also considered that microwave-assisted heating, non-thermal effects, and solvothermal conditions together with the effect of DEG solvent support the formation of "paperclip" architecture **[67]**. It is assumed that the final morphology of VO-C and VO-NC composites may also be a consequence of an arrangement between vanadium-oxo clusters and linkers in parent MOFs.

TEM images of VO-C and VO-NC composites are shown in **Fig. 9**. The VO-C composite (**Fig. 9(a)-(c)**) exhibits an amorphous structure of agglomerates consisted of VO_x/carbon nano-sheets. The thin morphology allows HRTEM imaging at an atomic scale. HRTEM image (**Figs. 9(c) and 14S**) reveals lattice fringes with distances of about 0.25 nm and 0.18 nm corresponding to the inter-plane spacing of (410) and (020) planes of orthorhombic V_2O_5, respectively **[85-87]**. Since observed particles are very small (below 5 nm) and their possible diffraction lines are proposed to be broad, they are not detected on the PXRD diffractogram **(Fig. 5(a)) [88]**. The VO-NC composite with the architecture of "paperclips" is displayed in **Fig. 9(d)-(f)**. In the case of the VO-NC "paperclip" sample no lattice fringes were detected **(Fig. 15S)**.

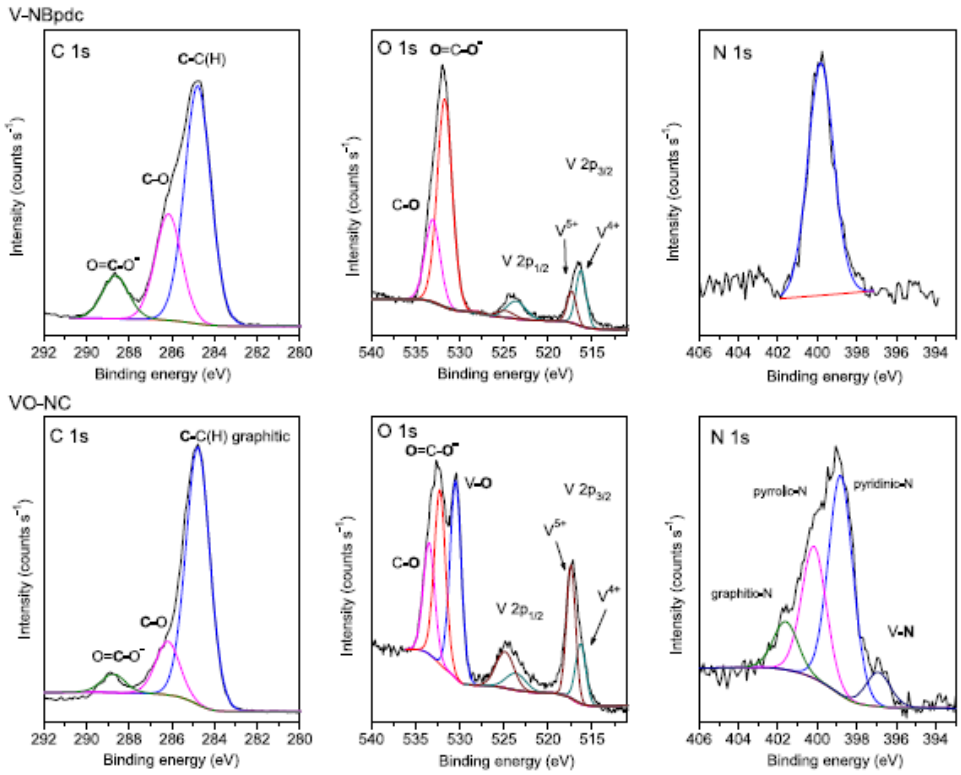

Fig. 7. XPS spectra of V-NBpdc MOF product (upper) and XPS spectra of MOF derived VO-NC composite (bottom).

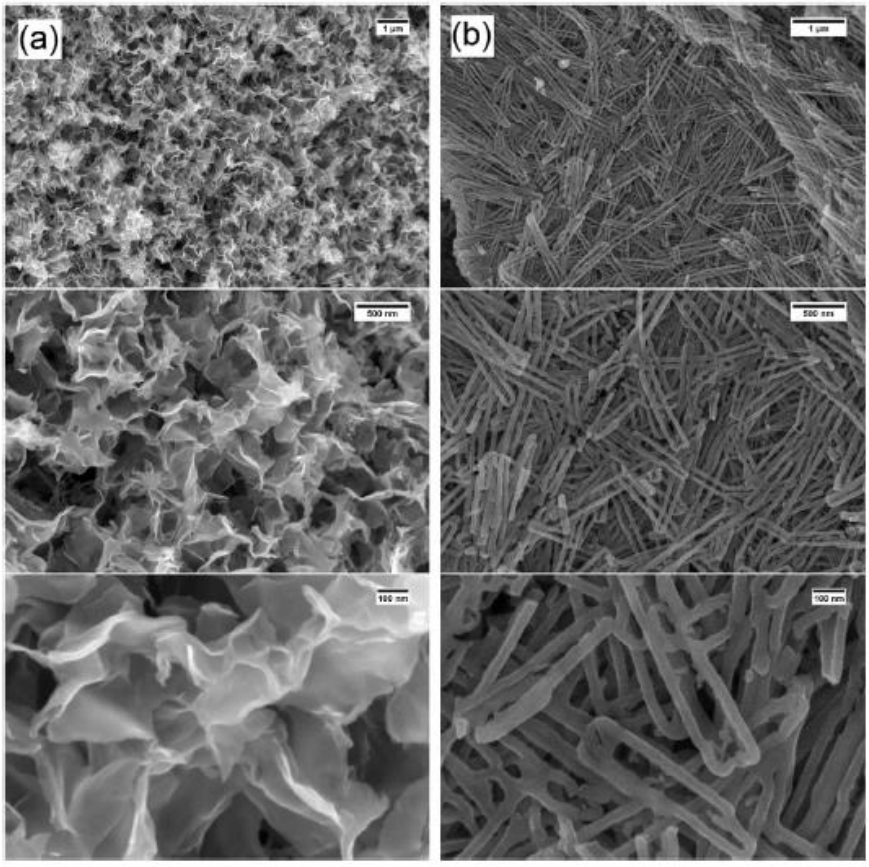

Fig. 8. SEM images of (a) sponge-like nano-sheet VO-C composite and (b) paperclip-like VO-NC nanocomposites.

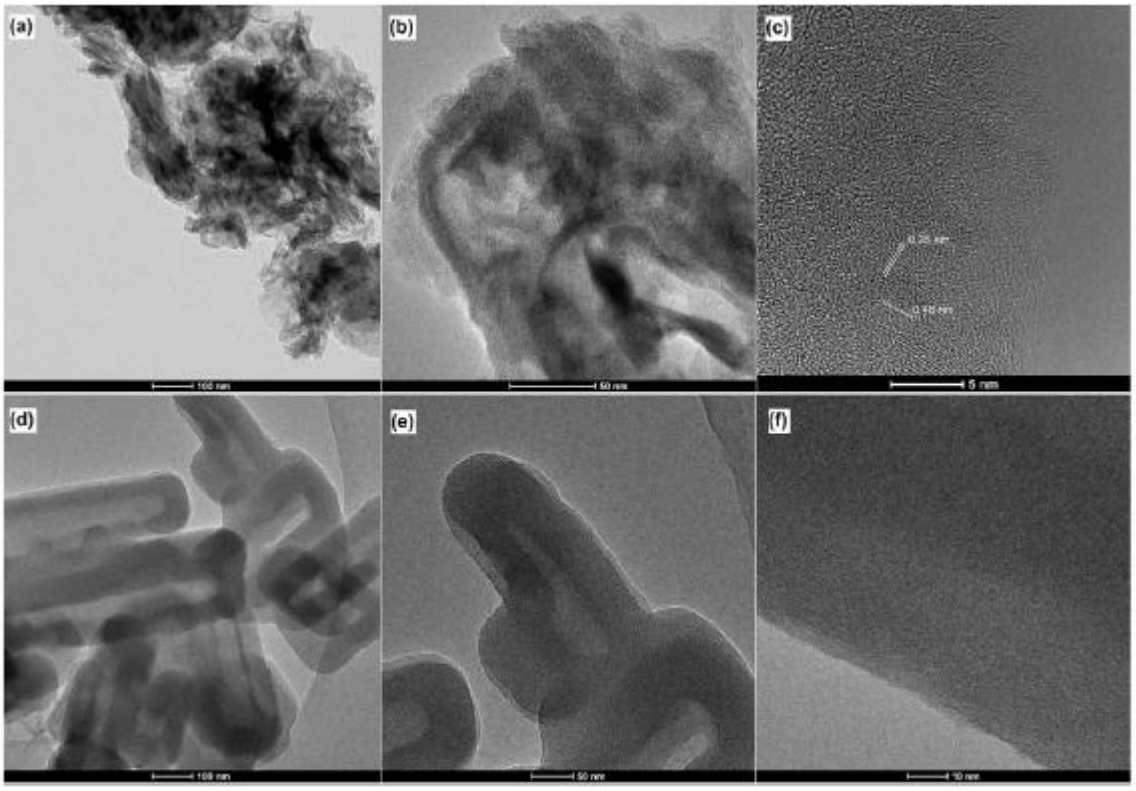

Fig. 9. TEM images of VO-C composite (a-c) and VO-NC composite (d-f) in different magnifications.

To investigate the homogeneity of the elemental distribution in VO-C and VO-NC composites, STEM-EDX elemental mapping was employed. As illustrated in **Fig. 10**, the distribution of vanadium and oxygen elements in the carbon matrix of VO-C composite is homogeneous. STEM-EDX elemental maps of VO-NC composite are shown in **Figs. 10 and 16S**. It can be concluded, that the homogeneous distribution of vanadium, oxygen, nitrogen, and carbon in the VO-NC composite is achieved. Based on the illustrated elemental maps it can be testified that carbonization of vanadium MOFs led to homogeneous carbon-based nanocomposites.

Nitrogen adsorption/desorption isotherms of vanadium MOF-derived composites VO-C and VO-NC are illustrated in **Fig. 11**. As displayed, isotherms are classified as type III, and nitrogen adsorption takes place at high p/p_0 pressures, which is characteristic for graphite-like materials **[89]**. Sample VO-C derived from V-Bpdc exhibited BET surface area 108 $m^2\ g^{-1}$ with the total pore volume 0.5 $cm^3\ g^{-1}$. In the case of the VO-NC sample, the surface area of 23 $m^2\ g^{-1}$ and the total pore volume of 0.2 $cm^3\ g^{-1}$ were observed. The low surface area of the VO-NC sample (23 $m^2\ g^{-1}$) in comparison to VO-C can be explained as a result of the linker contained in V-NBpdc MOF and its different morphology.

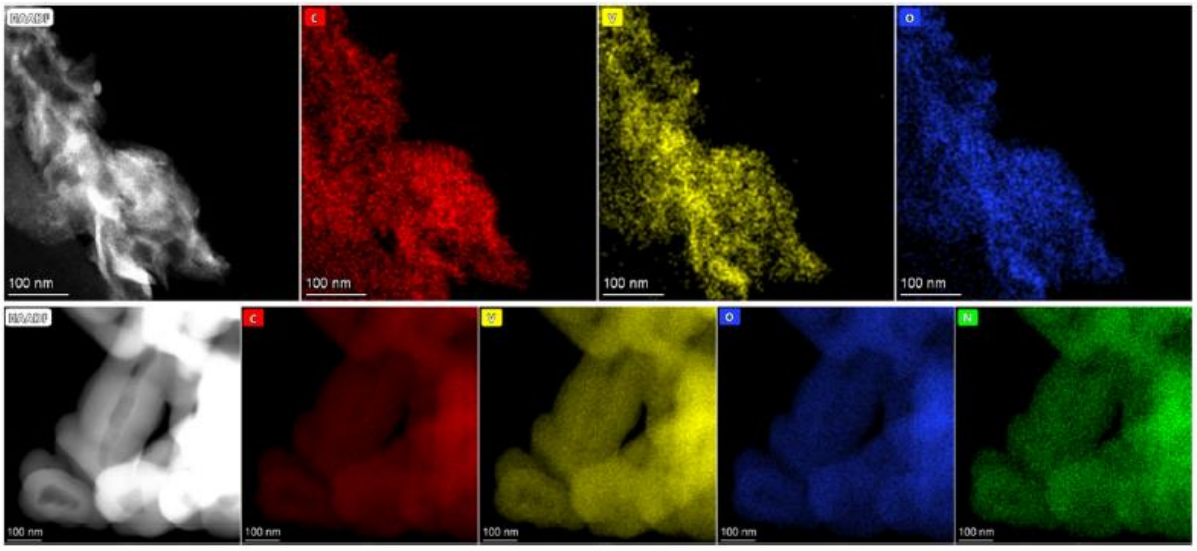

Fig. 10. STEM-HAADF images and corresponding-EDX elemental maps of VO-C (upper) and VO-NC (bottom) composites.

3.2. Electrochemical characterization

Since the application of composites of vanadium oxides and carbon or N-doped carbon in sodium-ion batteries has been reported recently **[30-32]**, in our work we investigated the electrochemical performance of VO_x/carbon-based nanocomposites. Vanadium MOF-derived nanocomposites VO-C and VO-NC with the nano-sheet and "paperclip" morphology, respectively, were used to prepare electrodes for the characterization of their electrochemical properties. To investigate the application potential of prepared nanocomposites, the electrodes were integrated into the SIB system. The first step of electrochemical characterization was cyclic voltammetry (CV) with a scan rate of 1 mV s^{-1}. The CV curves are shown in **Fig. 12** and according to the identical CV curve profiles of each sample, a stable electrochemical activity of both nanocomposite samples can be testified. According to a higher anodic/cathodic current, the VO-NC sample exhibited a higher electrochemical activity. The higher activity is also related to the higher capacity of the VO-NC sample (~215 mAh g^{-1}) compared to the VO-C sample with the capacity of ~145 mAh g^{-1} in the last cycle of CV. An absence of obvious peaks on CV curves can be explained as a consequence of the amorphous character of vanadium species (VO_x) in nanocomposites **(Fig. 5) [30,32,33]**. Such behavior has been observed in the work by Uchaker et al. **[33]**. As it has been reported, amorphous vanadium oxide exhibited a CV profile without the obvious peaks. However, its current response was higher than that for the crystalline material. It is assumed that such CV performance is tied to the broad energy dispersion of the sodiation sites, occupied via an apercolation mechanism, that allows a wide distribution of redox events **[33]**.

Electron impedance spectroscopy (EIS) measurements were performed to clarify the reason for the improvement of the electrochemical performance of the VO-NC composite. **Fig. 12** (b) shows the Nyquist plots of the VO-C and VO-NC nanocomposites and an equivalent circuit model. R_s represents the electrolyte and ohmic resistance of the cell. R_{ct} represents charge transfer resistance and CPE stands for double-layer capacitance. The value of charge transfer resistance of the VO-NC nanocomposite was 151.7 Ω which is lower than the charge transfer resistance of the VO-C nanocomposite (235.8 Ω). This improvement is achieved due to the presence of nitrogen which improves electron diffusion **[90]**. Because of the lower charge transfer resistance, the VO-NC nanocomposite exhibited higher electrochemical activity as observed on CV curves.

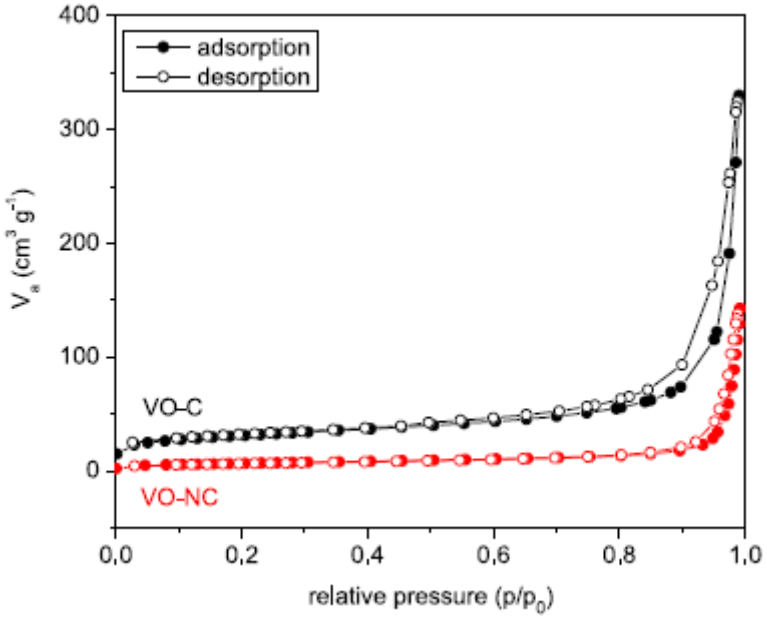

Fig. 11. Nitrogen adsorption/desorption isotherms of VO-C and VO-NC composites.

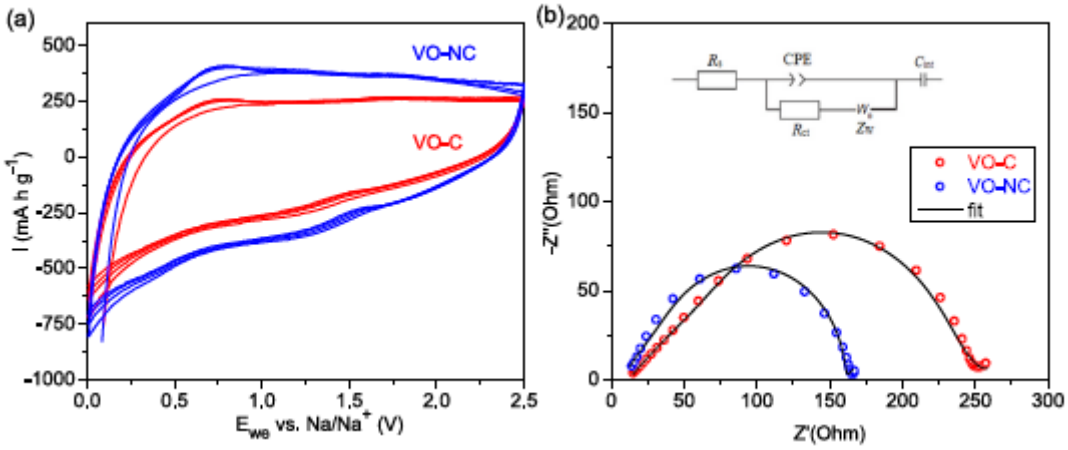

Fig. 12. (a) Cyclic voltammetry of VO-C and VO-NC nanocomposite samples vs. sodium at 1 mV s^{-1} (b) Nyquist plot of the VO-C and VO-NC nanocomposites and equivalent circuit model. The measured values are represented with the red and blue symbols for VO-C and VO-NC nanocomposites, respectively. Fitted plots are represented by solid black line. (For interpretation of the references to colour in this figure legend, the reader is referred to the Web version of this article.)

Capacitive or diffusion behavior was determined for both electrode materials by analyzing of b value using $i = av^b$2 formula. The b value obtained from **Fig. 13**(c) and (d) is 0.91 for VO-C electrode and 0.88 for VO-NC. Both electrodes show capacitive and diffusion-controlled behavior. In the case of VO-NC electrode the diffusion-controlled behavior is slightly higher. Normalized contribution ratio of capacitive and diffusion-controlled capacities at different scan rates is shown in **Fig. 13**(e) and (f). It is clear that VO-NC electrode has a greater proportion of diffusion-controlled capacity at all scan rates than VO-C electrode. Generally, both samples exhibit tendency to increase the contribution of the capacitive behavior at higher scan rate. Higher contribution of diffusion-controlled capacities at slower scan rate is beneficial from the point of view of higher capacity at lower C-rates. Similar behavior has

been observed by Liu **[32]** who studied vanadium oxide uniformly embedded into the highly defective carbon nanofibers.

As a next step, two charge/discharge cycles at 35 mA g^{-1} for the determination of capacity were performed. Both VO-C and VO-NC nanocomposites exhibited almost the same curve profiles without any stable plateau **(Fig. 14)**. In the case of VO-C and VO-NC samples, the capacity in the first cycle reached 204 mAh g^{-1} and 257 mAh g^{-1}, respectively. VO-C sample exhibited irreversible capacity loss of 23.6% in the first cycle and 15.4% in the second cycle **(Fig. 14)**, whereas, the irreversible capacity of the VO-NC nanocomposite sample reached 14.2% in the first cycle and 2.8% in the second cycle. This irreversible capacity of the VO-NC nanocomposite sample is very low compared to data that have been reported for vanadium oxide@N-doped carbon heterostructure (VNC) (58%, first cycle) and vanadium MIL-88B MOF-derived material (36%, first cycle) by Ren et al. **[30]** and Cai et al. **[56]**. V_2O_3/carbon nanocomposites published by An et al. **[91]** reached even in the second cycle irreversible capacity ~17%. Moreover, the irreversible capacity of the VO-NC sample is also lower in comparison to the hard carbon anode reported in the work of Kamiyama et al. **[92]** where the irreversible capacity of 25% was achieved.

Fig. 15(a) shows the cycling performance of the VO-C sample recorded at different C-rates. This electrode exhibited an initial discharge capacity of 152 mAh g^{-1} with a coulombic efficiency of 82%. During further cycling, the efficiency increased and varied around 97%. It is evident that with increasing C-rate, the capacity significantly decreases to 11 mAh g^{-1} in the last cycle at 2C. The capacity drop between the 20th cycle at 0.2C and the last cycle of all cycling was 20% and the capacity drop during overall cycling at different C-rates was 23%. The cycling performance of the VO-NC sample at different C-rates is shown in **Fig. 15(b)**. According to the higher activity observed during CV measurement (**Fig. 12**), the capacity of the VO-NC sample at the first cycle was 264 mAh g^{-1} with a coulombic efficiency of 96% which is significantly higher than values obtained for the VO-C sample. Coulombic efficiency during cycling further increased close to 99%. The VO-NC sample exhibited higher stability at a higher C-rate compared to the VO-C sample. The capacity at the last cycle at 2C was 35 mAh g^{-1}. The capacity drop between the 20th cycle at 0.2C and the last cycle of the whole cycling test of the VO-NC sample was 15% which is lower in comparison with the VO-C sample (20%). However, the overall capacity drop during cycling at different C-rate was 34% **(Fig. 15(b))**. The capacity drop after the first ten cycles of the VO-NC sample was more significant compared to the results of VO-C sample. However, during the rest of the cycling, the VO-NC sample was more stable and provided higher capacity within overall cycling at different C-rate **(Fig. 15)**. It is proposed that a better electrochemical behavior of VO-NC material is achieved because of the nitrogen element presence in the carbon matrix (11.1 wt%) **[29]**. It can also be taken into account that paperclip-like morphology with the rod-like architecture of particles may support the Na^+ transport.

The capacity and coulombic efficiency performance during cycling at 0.2C of the VO-C and VO-NC sample are shown in **Fig. 16.** The initial discharge capacity of the VO-C and VO-NC samples was 158 and 256 mAh g^{-1}, respectively. The instability of the capacity of the VO-NC electrode between the 2nd and 5th cycle can be attributed to the slight decomposition of the electrolyte at the higher voltage (above 2.3 V, **Fig. 14(b)**). This is also observable in the instability of coulombic efficiency. The coulombic efficiency of the VO-NC electrode was very stable during the rest of the cycling test and it was constant at around 99.5%. At the same time, the coulombic efficiency of the VO-NC sample was higher and more stable during overall cycling compared to the VO-C sample. These data are in correlation with the results from CV and EIS measurements **(Fig. 12).** Therefore, the lower the charge transfer resistance, the higher capacity, and better stability at high C-rates were provided by VO-NC nanocomposite.

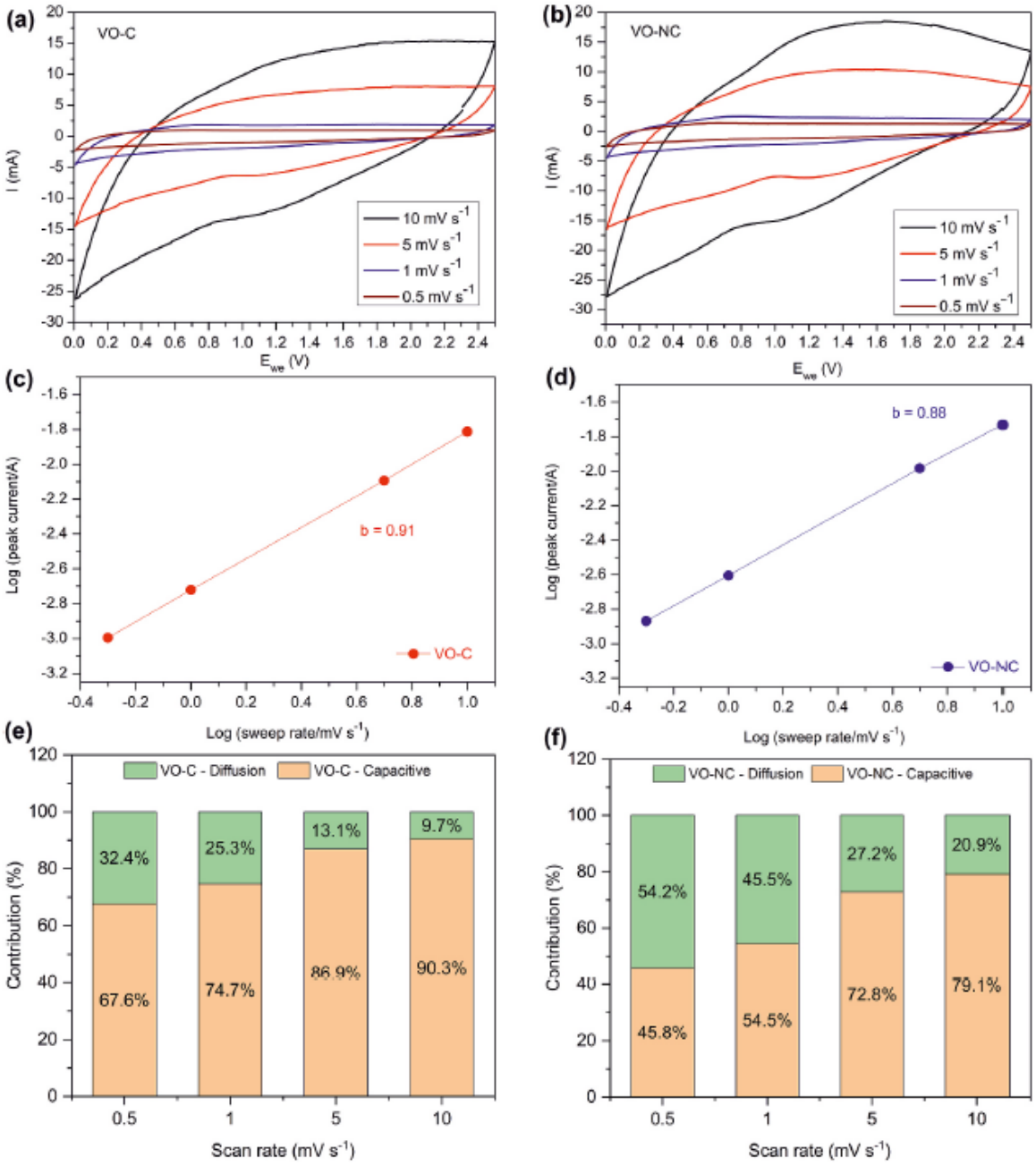

Fig. 13. (a, b) CV curves of VO-C and VO-NC at scan rates from 0.5 to 10 mV s^{-1}. (c, d) determination of the b value using plot of log (sweep rate) versus log (peak current) and the relationship between peak current and scan rate, and (e,f) the normalized contribution ratio of capacitive and diffusion-controlled capacities at different scan rates of VO-C and VO-NC nanocomposites.

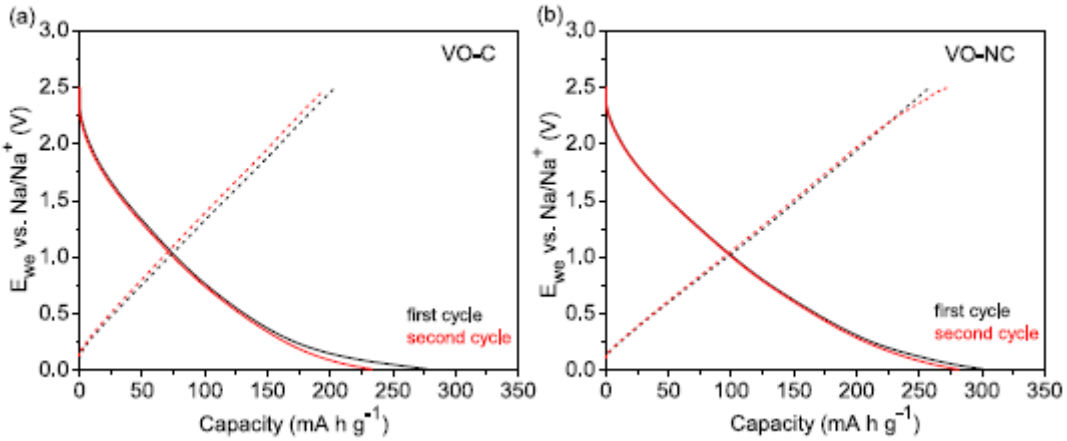

Fig. 14. Two charge/discharge cycles of (a) VO-C composite sample and (b) VO-NC nanocomposite recorded at 35 mA g^{-1}

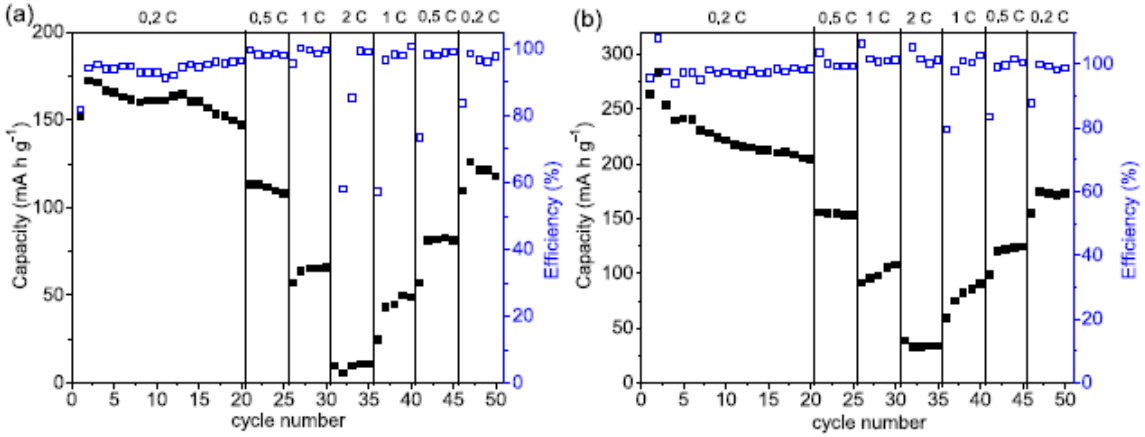

Fig. 15. The capacities achieved during the cycling of (a) VO-C and (b) VO-NC composite samples vs. sodium at different C-rates.

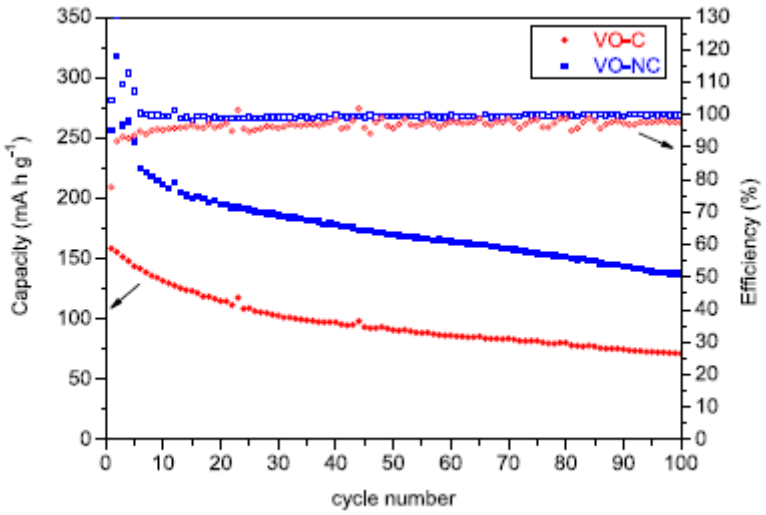

Fig. 16. The capacity and stability of VO-C and VO-NC composite-based electrodes within 100 cycles.

Over the 100 cycles, the VO-NC electrode displays a capacity of 137 mAh g^{-1}, almost double compared to the VO-C sample (71 mAh g^{-1}). Capacity retention during the overall cycling of the VO-C and VO-NC samples was 45% and 54%, respectively. In the case of V_2O_3/carbon nanocomposites reported by An et al. **[91]** the capacity retention after 100 cycles at 100 mA g^{-1} was 36%. Capacity retention from cycle 20th was 62% for the sample VO-C and 71% for the VO-NC sample. The VO-NC sample exhibited similar behavior compared to the previous cycling **(Fig. 16)**, and therefore a faster decrease in capacity at the beginning of cycling, and subsequently higher stability. To conclude the electrochemical performance results of VO-C and VO-NC nanocomposite samples, it has to be pointed out that VO-NC reached higher capacity and stability than the VO-C sample. This observation can be explained with the characteristic properties of the nitrogen-containing carbon matrix and morphology of the VO-NC sample. As reported, nitrogen doping of carbon structures increased conductivity and facilitated ion/electron transfer **[8]**. Moreover, the supporting effect of interconnected fiber-like architecture on charge transfer has been observed in the work of Fu et al. **[93]**, hence, such a promoting effect can be considered in the case of the VO-NC sample as well.

SEM images of electrode materials before and after charge/discharge cycling at different C-rates **(Fig. 15)** are depicted in **Fig. 17(a-d)**. The electrode material based on the VO-C nano-sheet composite before and after charge/discharge cycling is displayed in **Fig. 17(a) and (b)**, respectively. For better orientation, the VO-C nano-sheet composite is marked with yellow circles while the Super P carbon is labeled with red circles. It can be agreed that nano-sheet morphology is preserved after cycling and no significant changes of VO-C electrode material structure are observed. In the case of the electrode material containing a VO-NC sample with paperclip architecture **(Fig. 17(c and d))**, the SEM image after cycling demonstrates that the structure of the VO-NC nanocomposite has remained almost as same as before cycling. **Fig. 17(e)** shows XRD diffraction patterns of electrodes with VO-C and VO-NC nanocomposites after charge/discharge cycling **(Fig. 15)**. It is confirmed that no significant diffractions of the crystalline vanadium oxide phase occurred. The diffractions that are observed in diffracto-grams were assigned to silicon wafer substrate **[94]**, aluminum collector, and post-mortem XRD cell cover foil. This experiment confirmed that VO_x species are amorphous after charge/discharge cycles. Based on the results described above, it can be concluded, that structure and morphology of VO-C and VO-NC nanocomposites have exhibited stable behavior during charge/discharge cycling. Moreover, according to charge and discharge curves shown in **supplementary materials (Fig. 17 (S))** it is evident that sample remains in amorphous form because formation of a stable charging/discharging plateaus does not occur. In the case of V-CO sample we can observe an increase of hysteresis caused by an increase of internal resistance.

Comparison of VO-NC sample with VO_x-based materials presented in other articles is given in **Table 3**. VO-NC sample has a significantly lower irreversible capacity than other materials and a comparable capacity even though it is cycled in a smaller potential window than other materials. If the capacity achieved for other materials in the limited working window were taken into account, the achieved capacities would be smaller than in the case of the VO-NC sample. Stability during long term cycling is slightly worse compared with some of other reported materials, however, loading of active mass in the case of VO-NC sample is significantly higher **(Table 3)**.

Based on the reported data on vanadium oxide/carbon composites, the charge/discharge mechanism related to VO_x species in VO-C and VO-NC nanocomposites suggests that VO can convert into Na_2O and V species according to the following reaction equations: $VO + 2e^- + 2Na^+ \text{ ^ } Na_2O + V$ upon charging/discharging process **[30]**. Also, the intercalation of sodium into V_2O_5 species, described in the work by Ali et al. **[95]** via following equation: $V_2O_5 + x\ Na^+ \leftrightarrow Na_xV_2O_5$, may be considered during

charge/discharge process. Moreover, it has been reported recently **[31]** that in the case of amorphous vanadium oxi-de/MXene nanohybrid the electrochemical reactions during Na^+ insertion/extraction mechanism suggesting the oscillation of vanadium valence between V^{4+} and V^{5+} state.

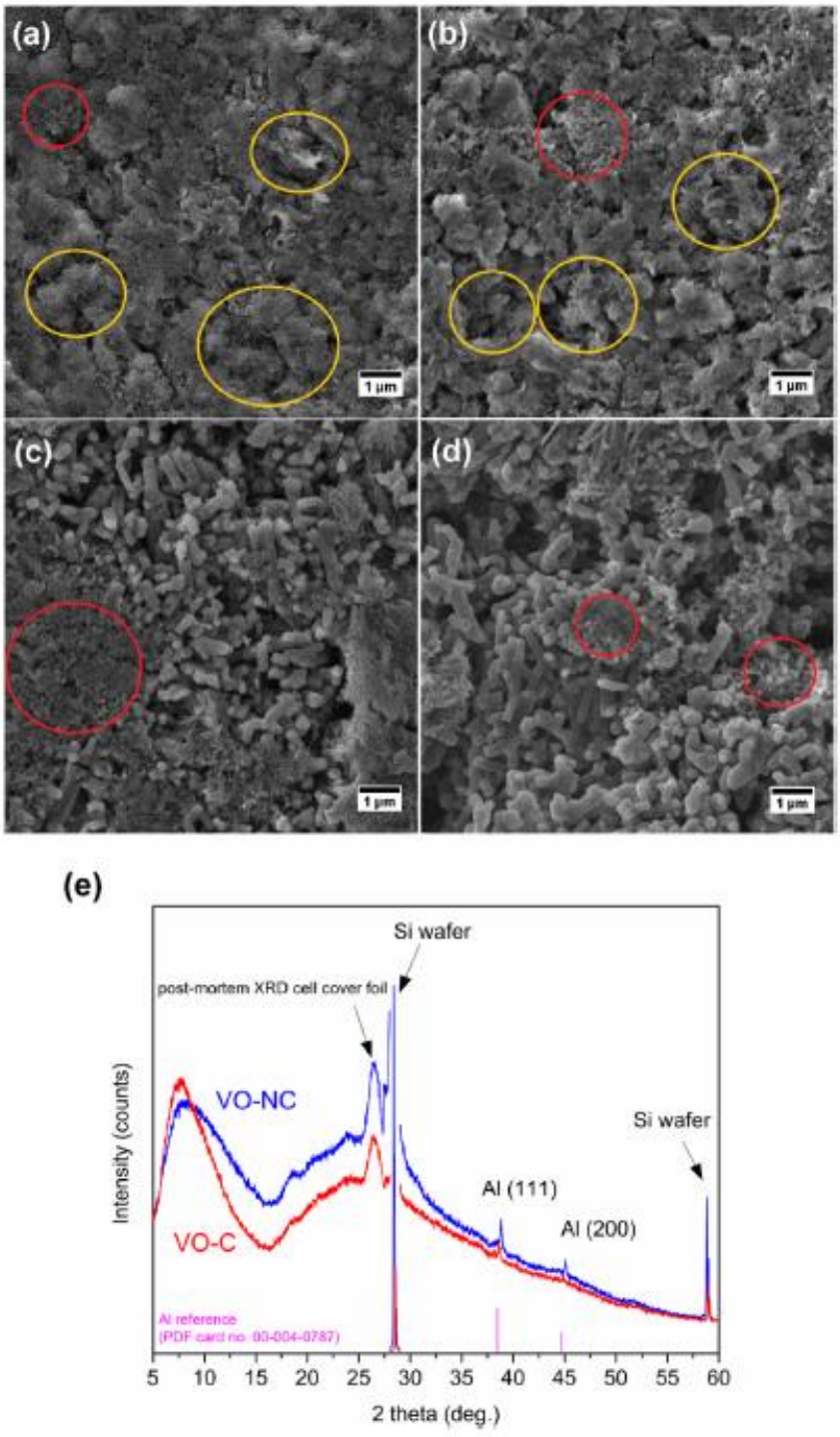

Fig. 17. SEM images of the electrode with VO-C nano-sheet sample (a) before and (b) after charge/ discharge cycling. SEM images of the electrode with VO-NC nanocomposite sample (c) before and (d) after charge/discharge cycling. The VO-C nanosheets are marked with yellow circles, Super P carbon is labeled with red circles. (e) XRD patterns of electrode materials after cycling (measured under argon atmosphere in post-mortem XRD cell). (For interpretation of the references to colour in this figure legend, the reader is referred to the Web version of this article.)

Furthermore, Ren et al. **[30]** have reported that the V-N bond can improve the electrochemical performance due to rapid charge transfer at the vanadium oxides/carbon interface. The N-doped carbon surface exhibits enhanced affinity to Na^+ ions and VO_x species. Thus, the interfacial V-N bonding between N-doped carbon and VO_x species exhibited a promoting effect on the charge transfer at the heterojunction interface. It is assumed that the same effect could support the charge transfer in the VO-NC sample.

4. Conclusion

In this work, a facile microwave-assisted polyol solvothermal synthesis of vanadium metal-organic frameworks (V-Bpdc and V-NBpdc) from vanadyl acetylacetonate precursor is presented. As organic linkers, biphenyl-4,4'-dicarboxylic and 2,2'-bipyridine-4,4'-dicarboxylic acid were used and the reaction was performed in diethylene glycol solvent at 230 °C. Prepared vanadium-based MOFs were carbonized at 600 °C in an argon atmosphere to obtain VO_x/carbon (VO-C) and VO_x/N-doped carbon (VO-NC) composites. It was found that the reported method provides the composites with interesting nano-sheet (VO-C) or "paperclip" (VO-NC) morphology with homogeneously distributed elemental composition. The VO-C nano-sheet thickness was 5-20 nm and the rod diameter in the case of VO-NC "paperclips" ranged from 35 to 70 nm. Both nanocomposite materials were electrochemically active at low potential under 2 V vs. Na^+. Because of the electrochemical activity, the VO-C and VO-NC can be used as anode materials for SIBs. Different morphology and nitrogen-containing carbon matrix of the VO-NC sample led to the improvement of the electrochemical properties of SIBs anode. A capacity of over 250 mAh g^{-1} was observed with a very low irreversible capacity under 15%. These properties make this material an interesting candidate for further use in advanced SIBs.

Table 3 Comparison of VO-NC sample performance with other VO_x-based materials.

Material	Ref.	C-rate	Capacity [mAh g^{-1}]	Irreversible capacity [%]	Number of cycles	Cycling drop [%]	Working window [V]	Loading [mg/ cm^2]
VO@N-doped carbon heterostructure	[30]	– 0.8C	272	57,5	100	10.6% (0.11% per cycle)	0.1–3.0	–
α-VO_x/V_2C nanohybrid	[31]	– 0.1–8C	310	–	60	19.4% (0.32% per cycle)	1.5-3.8	1.0–1.2
Porous shuttle-like V_2O_3/C	[56]	– 0.8C	257	35,9	100	15.6% (0.16% per cycle)	0.01–3.0	–
Amorphous vanadium oxide	[33]	0.2C	216	37	100	35.2% (0.35% per cycle)	1.5-3.8	–
VO_x@CNF600	[32]	– 0.3–16C	269	65,5	90	6.3%, include 1st cycle 66%	0.01–3.0	1
VO_x/N-doped C paperclip (VO-NC)	this work	0.2C	256	14,2	100	54% (0.53% per cycle)	0.01–2.5	2,7

References

[1] N. Yabuuchi, K. Kubota, M. Dahbi, S. Komaba, Research development on sodium-ion batteries, Chem. Rev. 114 (2014) 11636-11682, https://doi.org/10.1021/cr500192f.

[2] D. Kundu, E. Talaie, V. Duffort, L.F. Nazar, The emerging chemistry of sodium ion batteries for electrochemical energy storage, Angew. Chem. Int. Ed. 54 (2015) 3431-3448, https://doi.org/10.1002/anie.201410376.

[3] S.Y. Hong, Y. Kim, Y. Park, A. Choi, N.-S. Choi, K.T. Lee, Charge carriers in rechargeable batteries: Na ions vs. Li ions, Energy Environ. Sci. 6 (2013) 2067, https://doi.org/10.1039/c3ee40811f.

[4] Y. Liang, W.-H. Lai, Z. Miao, S.-L. Chou, Nanocomposite materials for the sodium-ion battery: a review, Small 14 (2018) 1702514, https://doi.org/10.1002/ smll.201702514.

[5] N. Nitta, F. Wu, J.T. Lee, G. Yushin, Li-ion battery materials: present and future, Mater. Today 18 (2015) 252-264, https://doi.org/10.1016/j.mattod.2014.10.040.

[6] H.D. Yoo, E. Markevich, G. Salitra, D. Sharon, D. Aurbach, On the challenge of developing advanced technologies for electrochemical energy storage and conversion, Mater. Today 17 (2014) 110-121, https://doi.org/10.1016/j. mattod.2014.02.014.

[7] M.-S. Balogun, Y. Luo, W. Qiu, P. Liu, Y. Tong, A review of carbon materials and their composites with alloy metals for sodium ion battery anodes, Carbon N. Y. 98 (2016) 162-178, https://doi.org/10.1016/j.carbon.2015.09.091.

[8] E. Wang, M. Chen, X. Guo, S. Chou, B. Zhong, S. Dou, Synthesis strategies and structural design of porous carbon-incorporated anodes for sodium-ion batteries, Small Methods 4 (2020) 1900163, https://doi.org/10.1002/smtd.201900163.

[9] L. Wang, Z. Wei, M. Mao, H. Wang, Y. Li, J. Ma, Metal oxide/graphene composite anode materials for sodium-ion batteries, Energy Storage Mater. 16 (2019) 434-454, https://doi.org/10.1016/j.ensm.2018.06.027.

[10] B.H. Hou, Y.Y. Wang, D.S. Liu, Z.Y. Gu, X. Feng, H. Fan, T. Zhang, L. Changli, X. L. Wu, N-doped carbon-coated Ni1.8Co1.2Se4 nanoaggregates encapsulated in N-doped carbon nanoboxes as advanced anode with outstanding high-rate and low-temperature performance for sodium-ion half/full batteries, Adv. Funct. Mater. 28 (2018) 1-9, https://doi.org/10.1002/adfm.201805444.

[11] D.A. Stevens, J.R. Dahn, The mechanisms of lithium and sodium insertion in carbon materials, J. Electrochem. Soc. 148 (2001) A803, https://doi.org/10.1149/ 1.1379565.

[12] H. Au, H. Alptekin, A.C.S. Jensen, E. Olsson, C.A. O'Keefe, T. Smith, M. Crespo-Ribadeneyra, T.F. Headen, C.P. Grey, Q. Cai, A.J. Drew, M.-M. Titirici, A revised mechanistic model for sodium insertion in hard carbons, Energy Environ. Sci. 13 (2020) 3469-3479, https://doi.org/10.1039/D0EE01363C.

[13] X. Li, H. Liang, X. Liu, R. Sun, Z. Qin, H. Fan, Y. Zhang, Ion-exchange strategy of CoS2/Sb2S3 hetero-structured nanocrystals encapsulated into 3D interpenetrating dual-carbon framework for high-performance Na+/K+ batteries, Chem. Eng. J. 425 (2021) 130657, https://doi.org/10.1016/j.cej.2021.130657.

[14] H. Fan, H. Yu, Y. Zhang, J. Guo, Z. Wang, H. Wang, N. Zhao, Y. Zheng, C. Du, Z. Dai, Q. Yan, J. Xu, 1D to 3D hierarchical iron selenide hollow nanocubes assembled from FeSe2@C core-shell nanorods for advanced sodium ion batteries, Energy Storage Mater. 10 (2018) 48-55, https://doi.org/10.1016/j. ensm.2017.08.006.

[15] Y. Lin, Z. Qiu, D. Li, S. Ullah, Y. Hai, H. Xin, W. Liao, B. Yang, H. Fan, J. Xu, C. Zhu, NiS2@CoS2 nanocrystals encapsulated in N-doped carbon nanocubes for high performance lithium/sodium ion batteries, Energy Storage Mater. 11 (2018) 67-74, https://doi.org/10.10Wj.ensm.2017.06.001.

[16] X. Zhou, Y.-G. Guo, Highly disordered carbon as a superior anode material for room-temperature sodium-ion batteries, Chemelectrochem 1 (2014) 83-86, https://doi.org/10.1002/celc.201300071.

[17] T. Chen, Y. Liu, L. Pan, T. Lu, Y. Yao, Z. Sun, D.H.C. Chua, Q. Chen, Electrospun carbon nanofibers as anode materials for sodium ion batteries with excellent cycle performance, J. Mater. Chem. A. 2 (2014) 4117, https://doi.org/10.1039/ c3ta14806h.

[18] S. Komaba, W. Murata, T. Ishikawa, N. Yabuuchi, T. Ozeki, T. Nakayama, A. Ogata, K. Gotoh, K. Fujiwara, Electrochemical Na insertion and solid electrolyte interphase for hard-carbon electrodes and application to Na-ion batteries, Adv. Funct. Mater. 21 (2011) 3859-3867, https://doi.org/10.1002/adim.201100854.

[19] X. Dou, I. Hasa, D. Saurel, C. Vaalma, L. Wu, D. Buchholz, D. Bresser, S. Komaba, S. Passerini, Hard carbons for sodium-ion batteries: structure, analysis, sustainability, and electrochemistry, Mater. Today 23 (2019) 87-104, https://doi. org/10.1016/j.mattod.2018.12.040.

[20] N. Zhang, B. Li, S. Li, S. Yang, Explored vanadium monoxide as a novel anode for lithium storage, Mater. Res. Express 5 (2018), 085502, https://doi.org/10.1088/ 2053-1591/aab72a.

[21] Y. Cheng, Y. Xia, Y. Chen, Q. Liu, T. Ge, L. Xu, L. Mai, Vanadium-based nanowires for sodium-ion batteries, Nanotechnology 30 (2019) 192001, https://doi.org/10.1088/1361-6528/aaff82.

[22] L.N. Wang, X. Wu, F.T. Wang, X. Chen, J. Xu, K.J. Huang, 1T-Phase MoS2 with large layer spacing supported on carbon cloth for high-performance Na+ storage, J. Colloid Interface Sci. 583 (2021) 579-585, https://doi.org/10.10Wj. jcis.2020.09.055.

[23] J. Xu, S. Zhang, Z. Wei, W. Yan, X. Wei, K. Huang, Orientated VSe2 nanoparticles anchored on N-doped hollow carbon sphere for high-stable aqueous energy application, J. Colloid Interface Sci. 585 (2021) 12-19, https://doi.org/10.1016/). jcis.2020.11.065.

[24] K. Tang, Y. Li, Y. Li, H. Cao, Z. Zhang, Y. Zhang, J. Yang, Self-reduced VO/VO x/ carbon nanofiber composite as binder-free electrode for supercapacitors, Electrochim. Acta 209 (2016) 709-718, https://doi.org/10.1016/). electacta.2016.05.051.

[25] C. Zhao, J. Cao, Y. Yang, W. Chen, J. Li, Facile synthesis of hierarchical porous VOx@carbon composites for supercapacitors, J. Colloid Interface Sci. 427 (2014) 73-79, https://doi.org/10.1016/j-jcis.2013.11.086.

[26] A. Viswanathan, A.N. Shetty, Reduced graphene oxide/vanadium pentoxide nanocomposite as electrode material for highly rate capable and durable supercapacitors, J. Energy Storage 27 (2020) 101103, https://doi.org/10.1016/). est.2019.101103.

[27] L. Xun, S. Gao, Y. Xu, X. Cheng, X. Zhang, H. Zhao, L. Huo, Synthesis of dandelionlike V 2 O 3/C composite with bicontinuous 3D hierarchical structures as an anode for high performance lithium ion batteries, Ceram. Int. 44 (2018) 14128-14135, https://doi.org/10.1016/j.ceramint.2018.05.012.

[28] P. Yu, X. Liu, L. Wang, C. Tian, H. Yu, H. Fu, Urchin-like V 2 O 3/C hollow nanosphere hybrid for high-capacity and long-cycle-life lithium storage, ACS Sustain. Chem. Eng. 5 (2017) 11238-11245, https://doi.org/10.1021/ acssuschemeng.7b01640.

[29] J. Wu, Z. Pan, Y. Zhang, B. Wang, H. Peng, The recent progress of nitrogen-doped carbon nanomaterials for electrochemical batteries, J. Mater. Chem. A. 6 (2018) 12932-12944, https://doi.org/10.1039/C8TA03968B.

[30] Q. Ren, N. Qin, B. Liu, Y. Yao, X. Zhao, Z. Deng, Y. Li, Y. Dong, D. Qian, B.-L. Su, W. Zhang, H.-E. Wang, An oxygen-deficient vanadium oxide@N-doped carbon heterostructure for sodium-ion

batteries: insights into the charge storage mechanism and enhanced reaction kinetics, J. Mater. Chem. A. 8 (2020) 3450-3458, https://doi.org/10.1039/C9TA11965E.

[31] W. Zhang, J. Peng, W. Hua, Y. Liu, J. Wang, Y. Liang, W. Lai, Y. Jiang, Y. Huang, W. Zhang, H. Yang, Y. Yang, L. Li, Z. Liu, L. Wang, S. Chou, Architecting amorphous vanadium oxide/MXene nanohybrid via tunable anodic oxidation for high-performance sodium-ion batteries, Adv. Energy Mater. 11 (2021) 2100757, https://doi.org/10.1002/aenm.202100757.

[32] T. Liu, L. Li, T. Yao, Y. Li, L. Zhu, F. Li, X. Han, Y. Cheng, H. Wang, Integrating amorphous vanadium oxide into carbon nanofibers via electrospinning as high-performance anodes for alkaline ion (Li+/Na+/K+) batteries, Electrochim. Acta 369 (2021) 137711, https://doi.org/10.10Wj.electacta.2020.137711.

[33] E. Uchaker, Y.Z. Zheng, S. Li, S.L. Candelaria, S. Hu, G.Z. Cao, Better than crystalline: amorphous vanadium oxide for sodium-ion batteries, J. Mater. Chem. A. 2 (2014) 18208-18214, https://doi.org/10.1039/C4TA03788J.

[34] L. Hu, Q. Chen, Hollow/porous nanostructures derived from nanoscale metal-organic frameworks towards high performance anodes for lithium-ion batteries, Nanoscale 6 (2014) 1236-1257, https://doi.org/10.1039/C3NR05192G.

[35] F. Zheng, G. Xia, Y. Yang, Q. Chen, MOF-derived ultrafine MnO nanocrystals embedded in a porous carbon matrix as high-performance anodes for lithium-ion batteries, Nanoscale 7 (2015) 9637-9645, https://doi.org/10.1039/C5NR00528K.

[36] B. Chen, G. Ma, Y. Zhu, Y. Xia, Metal-organic-frameworks derived cobalt embedded in various carbon structures as bifunctional electrocatalysts for oxygen reduction and evolution reactions, Sci. Rep. 7 (2017) 5266, https://doi.org/10.1038/s41598-017-05636-y.

[37] D. Skoda, T. Kazda, L. Munster, B. Hanulikova, A. Styskalik, P. Eloy, D.P. Debecker, J. Vilcakova, O. Cech, L. Simonikova, V. Kanicky, I. Kuritka, Microwave-assisted synthesis of platelet-like cobalt metal-organic framework, its transformation to porous layered cobalt-carbon nanocomposite discs and their utilization as anode materials in sodium-ion batteries, J. Energy Storage 27 (2020) 101113. https://linkinghub.elsevier.com/retrieve/pii/S2352152X19310783.

[38] W. Yang, X. Li, Y. Li, R. Zhu, H. Pang, Applications of metal-organic-framework-derived carbon materials, Adv. Mater. 1804740 (2018) 1804740, https://doi.org/ 10.1002/adma.201804740.

[39] J. Hwang, A. Ejsmont, R. Freund, J. Goscianska, B.V.K.J. Schmidt, S. Wuttke, Controlling the morphology of metal-organic frameworks and porous carbon materials: metal oxides as primary architecture-directing agents, Chem. Soc. Rev. (2020), https://doi.org/10.1039/C9CS00871C.

[40] H. Furukawa, K.E. Cordova, M. O'Keeffe, O.M. Yaghi, The chemistry and applications of metal-organic frameworks, Science 341 (80) (2013), https://doi. org/10.1126/science.1230444, 1230444-1230444.

[41] J. Liu, C. Woll, Surface-supported metal-organic framework thin films: fabrication methods, applications, and challenges, Chem. Soc. Rev. 46 (2017) 5730-5770, https://doi.org/10.1039/C7CS00315C.

[42] J.L.C. Rowsell, O.M. Yaghi, Metal-organic frameworks: a new class of porous materials, Microporous Mesoporous Mater. 73 (2004) 3-14, https://doi.org/ 10.1016/j.micromeso.2004.03.034.

[43] S. Yuan, L. Zou, J.-S. Qin, J. Li, L. Huang, L. Feng, X. Wang, M. Bosch, A. Alsalme, T. Cagin, H.-C. Zhou, Construction of hierarchically porous metal-organic frameworks through linker labilization, Nat. Commun. 8 (2017) 15356, https:// doi.org/10.1038/ncomms15356.

[44] E. Flage-Larsen, K. Thorshaug, Linker conformation effects on the band gap in metal-organic frameworks, Inorg. Chem. 53 (2014) 2569-2572, https://doi.org/ 10.1021/ic4028628.

[45] C.K. Lin, D. Zhao, W.Y. Gao, Z. Yang, J. Ye, T. Xu, Q. Ge, S. Ma, D.J. Liu, Tunability of band gaps in metal-organic frameworks, Inorg. Chem. 51 (2012) 9039-9044, https://doi.org/10.1021/ic301189m.

[46] P. Deria, J.E. Mondloch, O. Karagiaridi, W. Bury, J.T. Hupp, O.K. Farha, Beyond post-synthesis modification: evolution of metal-organic frameworks via building block replacement, Chem. Soc. Rev. 43 (2014) 5896-5912, https://doi.org/ 10.1039/C4CS00067F.

[47] W. Lu, Z. Wei, Z.-Y. Gu, T.-F. Liu, J. Park, J. Park, J. Tian, M. Zhang, Q. Zhang, T. Gentle III, M. Bosch, H.-C. Zhou, Tuning the structure and function of metal-organic frameworks via linker design, Chem. Soc. Rev. 43 (2014) 5561-5593, https://doi.org/10.1039/C4CS00003J.

[48] R.-Q. Zhong, R.-Q. Zou, M. Du, T. Yamada, G. Maruta, S. Takeda, J. Li, Q. Xu, Metal-organic frameworks of manganese(II) 4,4'-biphenyldicarboxylates: crystal structures, hydrogen adsorption, and magnetism properties, CrystEngComm 12 (2010) 677-681, https://doi.org/10.1039/B916168F.

[49] N.A. Khan, S.H. Jhung, Synthesis of metal-organic frameworks (MOFs) with microwave or ultrasound: rapid reaction, phase-selectivity, and size reduction, Coord. Chem. Rev. 285 (2015) 11-23, https://doi.org/10.10Wj.ccr.2014.10.008.

[50] R.F. Mendes, J. Rocha, F.A. Almeida Paz, Microwave synthesis of metal-organic frameworks, in: Met. Fram. Biomed. Appl., Elsevier, 2020, pp. 159-176, https:// doi.org/10.1016/B978-0-12-816984-1.00010-X.

[51] A. Phan, A.U. Czaja, F. Gándara, C.B. Knobler, O.M. Yaghi, Metal-organic frameworks of vanadium as catalysts for conversion of methane to acetic acid, Inorg. Chem. 50 (2011) 7388-7390, https://doi.org/10.1021/ic201396m.

[52] X. Wang, L. Liu, A.J. Jacobson, Intercalation of organic molecules into vanadium (IV) benzenedicarboxylate: adsorbate structure and selective absorption of organosulfur compounds, Angew. Chem. Int. Ed. 45 (2006) 6499-6503, https:// doi.org/10.1002/anie.200602556.

[53] W. Kaveevivitchai, A.J. Jacobson, Exploration of vanadium benzenedicarboxylate as a cathode for rechargeable lithium batteries, J. Power Sources 278 (2015) 265-273, https://doi.org/10.1016/jjpowsour.2014.12.094.

[54] Y. Yan, Y. Luo, J. Ma, B. Li, H. Xue, H. Pang, Facile synthesis of vanadium metal-organic frameworks for high-performance supercapacitors, Small 14 (2018) 1801815, https://doi.org/10.1002/smll.201801815.

[55] P. Van Der Voort, K. Leus, Y.-Y. Liu, M. Vandichel, V. Van Speybroeck, M. Waroquier, S. Biswas, Vanadium metal-organic frameworks: structures and applications, New J. Chem. 38 (2014) 1853-1867, https://doi.org/10.1039/ C3NJ01130E.

[56] Y. Cai, G. Fang, J. Zhou, S. Liu, Z. Luo, A. Pan, G. Cao, S. Liang, Metal-organic framework-derived porous shuttle-like vanadium oxides for sodium-ion battery application, Nano Res. 11 (2018) 449-463, https://doi.org/10.1007/s12274-017-1653-9.

[57] L. Kong, M. Zhong, Y. Liu, W. Xu, X.-H. Bu, Ultra-small V2O3 embedded N-doped porous carbon nanorods with superior cycle stability for sodium-ion capacitors, J. Power Sources 405 (2018) 37-44, https://doi.org/10.1016Zj. jpowsour.2018.10.016.

[58] Y. Ding, Y. Peng, W. Chen, Y. Niu, S. Wu, X. Zhang, L. Hu, V-MOF derived porous V2O5 nanoplates for high performance aqueous zinc ion battery, Appl. Surf. Sci. 493 (2019) 368-374, https://doi.org/10.10Wj.apsusc.2019.07.026.

[59] M. Liu, B. Su, Y. Tang, X. Jiang, A. Yu, Recent advances in nanostructured vanadium oxides and composites for energy conversion, Adv. Energy Mater. 7 (2017) 1700885, https://doi.org/10.1002/aenm.201700885.

[60] X.C. Xie, K.J. Huang, X. Wu, Metal-organic framework derived hollow materials for electrochemical energy storage, J. Mater. Chem. A. 6 (2018) 6754-6771, https:// doi.org/10.1039/c8ta00612a.

[61] X. Xie, K. Huang, X. Wu, N. Wu, Y. Xu, S. Zhang, C. Zhang, Binding hierarchical MoSe2 on MOF-derived N-doped carbon dodecahedron for fast and durable sodium-ion storage, Carbon N. Y. 169 (2020) 1-8, https://doi.org/10.1016/j. carbon.2020.07.010.

[62] O. Klvac, M.G. Ortiz, G. Fafilek, P. Vyroubal, R. Bayer, O. Cech, Ex-situ cell with positioner for XRD measurements in an inert atmosphere, ECS Trans 99 (2020) 333-339, https://doi.org/10.1149/09901.0333ecst.

[63] M. Jacquemin, M.J. Genet, E.M. Gaigneaux, D.P. Debecker, Calibration of the X-ray photoelectron spectroscopy binding energy scale for the characterization of heterogeneous catalysts: is everything really under control? ChemPhysChem 14 (2013) 3618-3626, https://doi.org/10.1002/cphc.201300411.

[64] D.A. Shirley, High-resolution X-ray photoemission spectrum of the valence bands of gold, Phys. Rev. B 5 (1972) 4709-4714, https://doi.org/10.1103/ PhysRevB.5.4709.

[65] S. Lowell, J.E. Shields, M.A. Thomas, M. Thommes, Surface area analysis from the Langmuir and BET theories, in: Charact. Porous Solids Powders Surf. Area, Pore Size Density, Springer Netherlands, 2004, pp. 58-81, https://doi.org/10.1007/978-1-4020-2303-3_5.

[66] J. Rouquerol, F. Rouquerol, P. Llewellyn, G. Maurin, K. Sing, Adsorption by Powders and Porous Solids Principles, Methodology and Applications, Academic Press, Amsterdam, 2014.

[67] A. de la Hoz, A. Díaz-Ortiz, A. Moreno, Microwaves in organic synthesis. Thermal and non-thermal microwave effects, Chem. Soc. Rev. 34 (2005) 164-178, https:// doi.org/10.1039/B411438H.

[68] G. Yang, S.-J. Park, Conventional and microwave hydrothermal synthesis and application of functional materials: a review, Materials (Basel) 12 (2019) 1177, https://doi.org/10.3390/ma12071177.

[69] G. Wenli, Z. Yue, L. Tongxiang, Preparation of copper coated carbon nanotubes by decomposition of Cu(II)acetylacetonate in hydrogen atmosphere, J. Mater. Sci. 41 (2006) 5462-5466, https://doi.org/10.1007/s10853-006-0309-z.

[70] L. Valenzano, B. Civalleri, S. Chavan, S. Bordiga, M.H. Nilsen, S. Jakobsen, K. P. Lillerud, C. Lamberti, Disclosing the complex structure of UiO-66 metal organic framework: a synergic combination of experiment and theory, Chem. Mater. 23 (2011) 1700-1718, https://doi.org/10.1021/cm1022882.

[71] R.A. Nyquist, C.L. Putzig, M.A. Leugers, Handbook of Infrared and Raman Spectra of Inorganic Compounds and Organic Salts, Elsevier Science, 1996. https://www. elsevier.com/books/handbook-of-infrared-and-raman-spectra-of-inorganic-compo unds-and-organic-salts/nyquist/978-0-12-523446-7. (Accessed 20 March 2020).

[72] S.K. Ghosh, R. Patra, S.P. Rath, Axial ligand coordination in sterically strained vanadyl porphyrins: synthesis, structure, and properties, Inorg. Chem. 47 (2008) 9848-9856, https://doi.org/10.1021/ic800714w.

[73] S. Chen, K. Li, K.S. Hui, J. Zhang, Regulation of lamellar structure of vanadium oxide via polyaniline intercalation for high-performance aqueous zinc-ion battery, Adv. Funct. Mater. 2003890 (2020) 2003890, https://doi.org/10.1002/ adfm.202003890.

[74] T.D. Bennett, A.K. Cheetham, Amorphous metal-organic frameworks, Acc. Chem. Res. 47 (2014) 1555-1562, https://doi.org/10.1021/ar5000314.

[75] D. Skoda, T. Kazda, L. Munster, B. Hanulikova, A. Styskalik, P. Eloy, D.P. Debecker, P. Vyroubal, L. Simonikova, I. Kuritka, Microwave-assisted synthesis of a manganese metal-organic framework and its transformation to porous MnO/ carbon nanocomposite utilized as a shuttle suppressing layer in lithium-sulfur batteries, J. Mater. Sci. 54 (2019) 14102-14122, https://doi.org/10.1007/s10853-019-03871-4.

[76] S. Yan, K.P. Abhilash, L. Tang, M. Yang, Y. Ma, Q. Xia, Q. Guo, H. Xia, Research advances of amorphous metal oxides in electrochemical energy storage and conversion, Small 15 (2018) 1804371, https://doi.org/10.1002/smll.201804371.

[77] Y.-Y. Liu, S. Couck, M. Vandichel, M. Grzywa, K. Leus, S. Biswas, D. Volkmer, J. Gascon, F. Kapteijn, J.F.M. Denayer, M. Waroquier, V. Van Speybroeck, P. Van Der Voort, New V IV -based metal-organic framework having framework flexibility and high CO 2 adsorption capacity, Inorg. Chem. 52 (2013) 113-120, https://doi. org/10.1021/ic301338a.

[78] M.C. Biesinger, L.W.M. Lau, A.R. Gerson, R.S.C. Smart, Resolving surface chemical states in XPS analysis of first row transition metals, oxides and hydroxides: Sc, Ti, V, Cu and Zn, Appl. Surf. Sci. 257 (2010) 887-898, https://doi.org/10.1016/j. apsusc.2010.07.086.

[79] S. Ma, J. Liang, J. Zhao, B. Xu, Synthesis, characterization and growth mechanism of flower-like vanadium carbide hierarchical nanocrystals, CrystEngComm 12 (2010) 750-754, https://doi.org/10.1039/B913278N.

[80] P. Ayala, A. Gruneis, T. Gemming, D. Grimm, C. Kramberger, M.H. Rummeli, F. L. Freire, H. Kuzmany, R. Pfeiffer, A. Barreiro, B. Buchner, T. Pichler, Tailoring N-doped single and double wall carbon nanotubes from a nondiluted carbon/nitrogen feedstock, J. Phys. Chem. C 111 (2007) 2879-2884, https://doi.org/10.1021/ jp0658288.

[81] M.R. Maurya, Development of the coordination chemistry of vanadium through bis (acetylacetonato)oxovanadium(IV): synthesis, reactivity and structural aspects, Coord. Chem. Rev. 237 (2003) 163-181, https://doi.org/10.1016/S0010-8545(02) 00293-X.

[82] S.G. Brand, N. Edelstein, C.J. Hawkins, G. Shalimoff, M.R. Snow, E.R.T. Tiekink, An oxo-bridged binuclear vanadium(III) 2,2'-bipyridine complex and its vanadium(IV) and vanadium(V) oxidation products, Inorg. Chem. 29 (1990) 434-438, https:// doi.org/10.1021/ic00328a018.

[83] B. Long, M.-S. Balogun, L. Luo, Y. Luo, W. Qiu, S. Song, L. Zhang, Y. Tong, Encapsulated vanadium-based hybrids in amorphous N-doped carbon matrix as anode materials for lithium-ion batteries, Small 13 (2017) 1702081, https://doi. org/10.1002/smll.201702081.

[84] P. Lazar, R. Mach, M. Otyepka, Spectroscopic fingerprints of graphitic, pyrrolic, pyridinic, and chemisorbed nitrogen in N-doped graphene, J. Phys. Chem. C 123 (2019) 10695-10702, https://doi.org/10.1021/acs.jpcc.9b02163.

[85] K. Zhu, C. Zhang, S. Guo, H. Yu, K. Liao, G. Chen, Y. Wei, H. Zhou, Sponge-like cathode material self-assembled from two-dimensional V 2 O 5 nanosheets for sodium-ion batteries, Chemelectrochem 2 (2015) 1660-1664, https://doi.org/ 10.1002/celc.201500240.

[86] L. Cao, J. Zhu, Y. Li, P. Xiao, Y. Zhang, S. Zhang, S. Yang, Ultrathin singlecrystalline vanadium pentoxide nanoribbon constructed 3D networks for superior energy storage, J. Mater. Chem. A. 2 (2014) 13136-13142, https://doi.org/ 10.1039/C4TA02229G.

[87] J. Zhao, H. Ren, Q. Liang, D. Yuan, S. Xi, C. Wu, W. Manalastas, J. Ma, W. Fang, Y. Zheng, C.-F. Du, M. Srinivasan, Q. Yan, High-performance flexible quasi-solid-state zinc-ion batteries with layer-expanded vanadium oxide cathode and zinc/ stainless steel mesh composite anode, Nano Energy 62 (2019) 94-102, https://doi. org/10.1016/j.nanoen.2019.05.010.

[88] M. Chiku, H. Takeda, S. Matsumura, E. Higuchi, H. Inoue, Amorphous vanadium oxide/carbon composite positive electrode for rechargeable aluminum battery, ACS Appl. Mater. Interfaces 7 (2015) 24385-24389, https://doi.org/10.1021/ acsami.5b06420.

[89] T. Qiu, J.-G. Yang, X.-J. Bai, Y.-L. Wang, The preparation of synthetic graphite materials with hierarchical pores from lignite by one-step impregnation and their characterization as dye absorbents, RSC Adv. 9 (2019) 12737-12746, https://doi.org/10.1039/C9RA00343F.

[90] X. Wang, J. Huang, J. Li, L. Cao, W. Hao, Z. Xu, Improved Na storage performance with the involvement of nitrogen-doped conductive carbon into WS 2 nanosheets, ACS Appl. Mater. Interfaces 8 (2016) 23899-23908, https://doi.org/10.1021/ acsami.6b06032.

[91] X. An, H. Yang, Y. Wang, Y. Tang, S. Liang, A. Pan, G. Cao, Hydrothermal synthesis of coherent porous V2O3/carbon nanocomposites for high-performance lithium-and sodium-ion batteries, Sci. China Mater. 60 (2017) 717-727, https://doi.org/ 10.1007/s40843-017-9054-0.

[92] A. Kamiyama, K. Kubota, T. Nakano, S. Fujimura, S. Shiraishi, H. Tsukada, S. Komaba, High-capacity hard carbon synthesized from macroporous phenolic resin for sodium-ion and potassium-ion battery, ACS Appl. Energy Mater. 3 (2020) 135-140, https://doi.org/10.1021/acsaem.9b01972.

[93] L. Fu, K. Tang, K. Song, P.A. van Aken, Y. Yu, J. Maier, Nitrogen doped porous carbon fibres as anode materials for sodium ion batteries with excellent rate performance, Nanoscale 6 (2014) 1384-1389, https://doi.org/10.1039/ C3NR05374A.

[94] I.A. Tarasov, I.A. Yakovlev, M.S. Molokeev, M. Rautskii, I.V. Nemtsev, S. N. Varnakov, S.G. Ovchinnikov, Growth of a-FeSi2 nanocrystals on si(100) with Au catalyst, Mater. Lett. 168 (2016) 90-94, https://doi.org/10.1016/j. matlet.2016.01.033.

[95] G. Ali, J. Lee, S.H. Oh, B.W. Cho, K.-W. Nam, K.Y. Chung, Investigation of the Na intercalation mechanism into nanosized V 2 O 5/C composite cathode material for Na-ion batteries, ACS Appl. Mater. Interfaces 8 (2016) 6032-6039, https://doi. org/10.1021/acsami.5b11954.